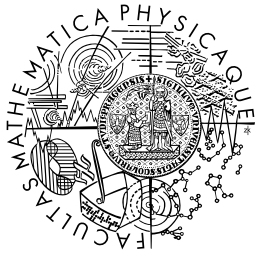

FACULTY
OF MATHEMATICS
AND PHYSICS
Charles University

MASTER THESIS

Jiří Volný

Transport properties of CuMnAs single crystal

Department of Condensed Matter Physics

Supervisor of the master thesis: RNDr. Klára Uhlířová, Ph.D.

Study programme: Physics

Study branch: Physics of condensed matter and materials

Prague 2021

I declare that I carried out this master thesis independently, and only with the cited sources, literature and other professional sources. It has not been used to obtain another or the same degree.

I understand that my work relates to the rights and obligations under the Act No. 121/2000 Sb., the Copyright Act, as amended, in particular the fact that the Charles University has the right to conclude a license agreement on the use of this work as a school work pursuant to Section 60 subsection 1 of the Copyright Act.

In ..... date ....

Author's signature

In this place I would like to thank my supervisor RNDr. Klára Uhlířová, Ph.D. for her guidance, help, provision of the CuMnAs polycrystalls and most of all patience with my many missteps. My thanks go to Dr. Karel Výborný for his comments and introduction to Stoner-Wohlfarth model. RNDr. David Wagenknecht, Ph.D. for the ab-initio calculations of resistivity and anisotropic magnetoresistance. Elen Duverger-Nédellec, Ph.D. for the single crystal diffraction and RNDr. Petr Harcuba, Ph.D. for the sample orientation by an EBSD. I want to thank department of Surface and Plasma Physics for providing the access to focused ion beam and RNDr. Jaroslava Nováková, Ph.D. for troubleshooting with focused ion beam. Experiments were performed in MGML (mgml.eu), which is supported within the program of Czech Research Infrastructures (project no. LM2018096). The author acknowledge the assistance provided by the Research Infrastructure NanoEnviCz, supported by the Ministry of Education, Youth and Sports of the Czech Republic under Project No. LM2018124. Last but not least I would like to thank my friends and family for moral support.

Title: Transport properties of CuMnAs single crystal

Author: Jiří Volný

Department: Department of Condensed Matter Physics

Supervisor: RNDr. Klára Uhlířová, Ph.D., Department of Condensed matter physics

Abstract: Electrical transport measurement of small, irregular shape sample is difficult task. In order to overcome these limitations, this thesis employed a focused ion beam microfabrication. Process of microfabrication is successfully tested on a room temperature antiferromagnet CuMnAs. Temperature dependence resistivity and magnetoresistance of tetragonal bulk CuMnAs single crystal is found to be strongly anisotropic due to layered structure and magnetic order. Anisotropic magnetoresistance shows two fold symmetry and reached a magnitude of ~ 0.12 %. Employing the phenomenological Stoner-Wohlfarth we conclude that the sample has uniaxial magnetic anisotropy with an easy axis not pointing along any principal crystallographic direction and behaves like a two domain antiferromagnet.

Keywords: Focused Ion Beam, Anisotropy, Antiferromagnet

Contents

Introduction

Introduction of an antiferromagnetic (AFM) materials into the field of spintronics marked its new era [1]. Apart from the commonly used ferromagnets (FM), net magnetization of AFM is zero. This makes it difficult for writing and reading of an information. On the other hand they offer advantages in a form of larger insensitivity to the external magnetic field, absence of a stray field and faster dynamics.

One of the most studied candidate for AFM spintronics usage is CuMnAs in a tetragonal form. Its locally broken symmetry on Mn sites allows for manipulation of magnetic moment using Néel order spin orbit torque [2]. The information is stored in two different orientation of magnetic moments. They are either parallel or perpendicular to the electrical current (fig. 1). Such effective manipulation of magnetic moments have been successfully demonstrated on the thin films of this compound. For the reading, anisotropic magnetoresistance is being used.

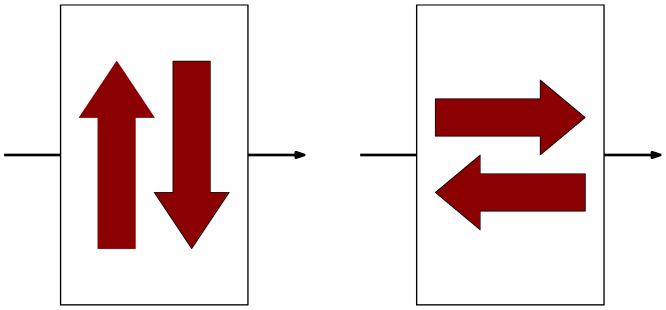

Figure 1: Simple scheme of an antiferromagnetic memory. Memory states are represented by a different orientation of spins (red arrow) in regards to the electrical current (black arrow). The resistance is higher for the state representing "1".

Even though the main application potential lies in a form of thin layer, bulk materials represent more suitable playground for a theoretical research due to lack of various parasitic physical phenomena (interface effects, surface, thickness, ...) as seen in thin layers. In the bulk form CuMnAs crystallizes in the orthorombic structure [3] [4]. The tetragonal modification of the bulk CuMnAs has been believed to be stabilized only in the form of thin layers. However it has been recently shown that the tetragonal modification is stabilized by a deviation in the 1-1-1 stoichiometry to the Cu rich side by a few atomic % [5].

This work is focused on transport properties of bulk CuMnAs single crystal in its tetragonal modification, which was not studied before. Yet, no sufficiently large CuMnAs single crystal has been available. Therefore a special technique for precise sample fabrication has been used. The transport properties are studied on a samples of dimensions of several tens of microns prepared by focused ion beam micromachining. Such device fabrication allows for precise control of orientation which is crucial for study of highly anistropic materials such as CuMnAs. Beside temperature dependence of electrical resistance and magnetoresitance an anisotropic magnetoresistance is studied and its origin is

further discussed by means of Stoner-Wohlfhart model.

This thesis is, beside introduction, divided into 5 chapters. In Chapter 1 - Theoretical background, necessary theoretical background in the scope of this thesis results is explained. Chapter 2 - Experimental methods gives an overview of used experimental instruments and techniques. Chapter 3 - Physical properties of CuMnAs present so far published results on this compound. In the Chapter 4 - Sample preparation, basics of focused ion beam microfabrication are explained. This is followed by a Chapter 5 - Results and discussion where the outcomes of the work are to be seen. Chapter - Conclusion sums up the main results of this work.

1. Theoretical background

1.1 Magnetism

Magnetic properties of solids are associated with its electronic structure. Magnetic moment of the nuclei is usually neglected as the magnetic moment is inversely proportional to the mass of a particle i.e. $\mu \sim 1/m$ [6] (magnetic moments of the nuclei are about 10^3 lower than the ones of electrons). Magnetic moment of free atom consist of three contributions: spin momentum of its electrons, orbital momentum of electrons and change of the electron orbital momentum induced by external magnetic field. The first two cases represent paramagnetic contribution while the last one is responsible for diamagnetism.

One of the fundamental property of materials is its magnetic susceptibility χ defined as [7]

$$\chi = \frac{dM}{dH} \tag{1.1}$$

According to the sign and magnitude of the χ we can distinguish between diamagnets, paramagnets and ferromagnets.

Diamagnetism

Diamagnetism is quantum mechanical effect which is a property of every material. Diamagnetism is characterized with $\chi < 0$. In case the electronic shells of individual ions in solid are filled, than the spin, orbital and total momentum are equal to zero [7] and the expression for susceptibility takes form [7]

$$\chi = -\frac{\mu_0 N Z e^2}{6m} < r^2 > \tag{1.2}$$

where μ_0 is vacuum permeability, N is number of electrons in unitary volume, e is charge of an electron, m is its mass, Z is number of electrons in atom and $< r^2 >$ is mean quadratic distance of electron from its nucleus. This is known as Langevin diamagnetic susceptibility (sometimes we can find the term Larmor diamagnetic susceptibility [7]). In metallic system, it is necessary to add additional term which corresponds to the orbital diamagnetism of free electrons. This is called Landau diamagnetic susceptibility and is given by [8]

$$\chi_L = \frac{\mu_0 \mu_B^2 g(E_F)}{3} \tag{1.3}$$

where $g(E_F)$ is number of states on Fermi level. As seen from eq. 1.2, 1.3, both Langevin and Landau diamagnetism are independent on temperature and external magnetic field.

Paramagnetism

Paramagnetism is consequence of partially filled electronic shells of ions in solid. Paramagnetism is characterized by $\chi > 0$. In case the shell have the total

angular momentum J=0. Then we speak of Van Vleck paramagnetism with its susceptibility given by term [7]

$$2n_i\mu_B^2 \sum_n \frac{|<0|\mu_B \mathbf{H}\cdot(\mathbf{L}+g_0\mathbf{S})>|^2}{E_n - E_0} \tag{1.4}$$

where n_i is number of ions in unitary volume, $\mathbf{L}$ is orbital momentum and $\mathbf{S}$ is spin momentum.

If we consider J$\neq$ 0. The susceptibility takes form of Curie's law [7]

$$\chi = \frac{C}{T} \tag{1.5}$$

where C is Curie constant and T is thermodynamic temperature. This paramagnetic susceptibility is temperature dependent and diverges at 0 K.

Beside Van Vleck contribution, metallic systems contain additional paramagnetic term which corresponds to the paramagnetism of conduction electrons. Application of external magnetic field tends to increase of the density of electrons with spin antiparallel to the external magnetic field and decreases the density of electron with spin parallel to the external magnetic field. This gives rise to a magnetization M of the conduction electrons

$$M = \mu_b(n_\uparrow - n_\downarrow) \tag{1.6}$$

which yields into a so called Pauli paramagnetic susceptibility χ_P which is χ_P =-3χ_L [7]

$$\chi_P = \mu_0\mu_B^2 g(E_F) \tag{1.7}$$

1.1.1 Magnetic ordering

Long range magnetic ordering is conditioned by a sufficient exchange interaction Jbetween individual magnetic moments. Exchange interaction is purely quantum mechanical effect and its origin can be traced to an electrostatic interaction between neighboring electrons acting together with Pauli exclusion principle [7]. Depending on the direction and size of individual magnetic moment we distinguish between different magnetically ordered states. Most important being ferromagnetism (FM), antiferromagnetism (AFM) and ferrimagnet [8] [7].

Magnetic ordering manifest itself bellow critical temperature. Above such temperatures the thermal fluctuations are large enough to overcome the exchange field. The long range mangetic ordering is destroyed and the material is in paramagnetic state. The temperature dependence of susceptibility for ferromagnets can be expresses in a form of Curie-Weiss Law [7]

$$\chi = \frac{C}{T - T_c} \tag{1.8}$$

where T_c is Curie temperature. In the case of antiferromagnets the Curie temperature is substituted by Néel temperature -T_N. As the susceptibility diverges at T_c (T_N) it is usual to plot inverse susceptibility i.e $1/\chi$. In the case of AFM we observe peak at T_N. Typical susceptibility for paramagnets, FM and AFM is plotted in fig. 1.1.

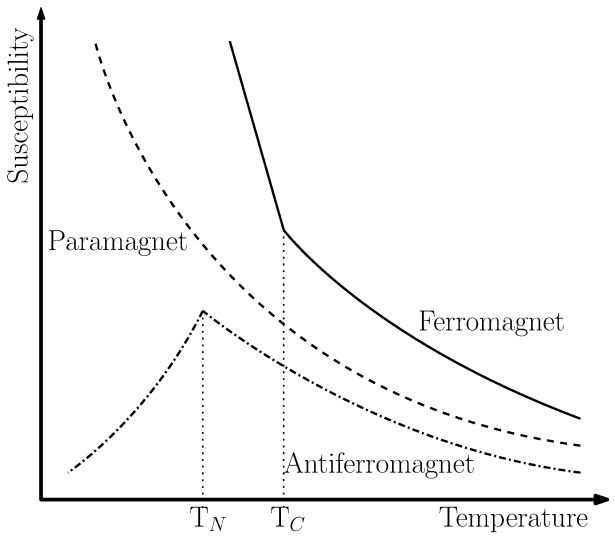

Figure 1.1: Temperature dependence of susceptibility of paramagnets, ferromagnets and antiferromagnets. The vertical dot lines denotes Curie (T_c) and Neél temperature (T_N). Drawn according to [7]

.

1.1.2 Magnetic anisotropy

Magnetic properties of solids are dependent on crystallographic direction. Magnetic moments in solids tends to align along some fixed direction. So called easy axis. This behavior is generally represented by an anisotropic energy E_a which, for the uniaxial (one easy axis) anisotropy, can be written in a following form [8]

$$E_a = K_u sin^2(\phi) \tag{1.9}$$

where K_u is an anisotropy constant and ϕ is an angle between the direction of magnetization and easy axis. Magnetic anisotropy is temperature dependent and it vanishes at transition temperature in the presence of no external field [8].

Most commonly the source of the anisotropy is related either to the shape of the sample (shape anisotropy), to the crystal structure (magnetocrystalline anisotropy) or it can be induced by an atomic or micro size texture [8].

Magnetocrystalline anisotropy

Apart from the later cases magnetocrystalline anisotropy is inherent property of the material. For single crystals in an external magnetic field we may observe different approach to saturation when measured along unequal crystallographic directions. For example in magnetite (fcc structure) as can be seen at fig. 1.2 we observe $\langle 100 \rangle$ as an easy axis while the saturation occurs along $\langle 111 \rangle$ at much higher magnetic field (hard axis).

The expression for anisotropy energy E_a differs for different symmetries:

$$\begin{aligned}
\text{Cubic} \quad E_a = \; & K_{1c}\alpha_1^2\alpha_2^2 + \alpha_2^2\alpha_3^2 + \alpha_3^2\alpha_1^2 + K_{2c}(\alpha_1^2\alpha_2^2\alpha_3^2) \\
\text{Tetragonal} \quad E_a = \; & K_1 \sin^2\phi + K_2 \sin^4\psi + K_2^{'} \sin^2\phi \cos 4\psi + K_3 \sin^6\phi \\
& + K_3^{'} \sin^6\phi \sin 4\psi \\
\text{Hexagonal} \quad E_a = \; & K_1 \sin^2\phi + K_2 \sin^4\phi + K_3 \sin^6\phi + K_3^{'} \sin^6\phi \sin 6\psi
\end{aligned}$$

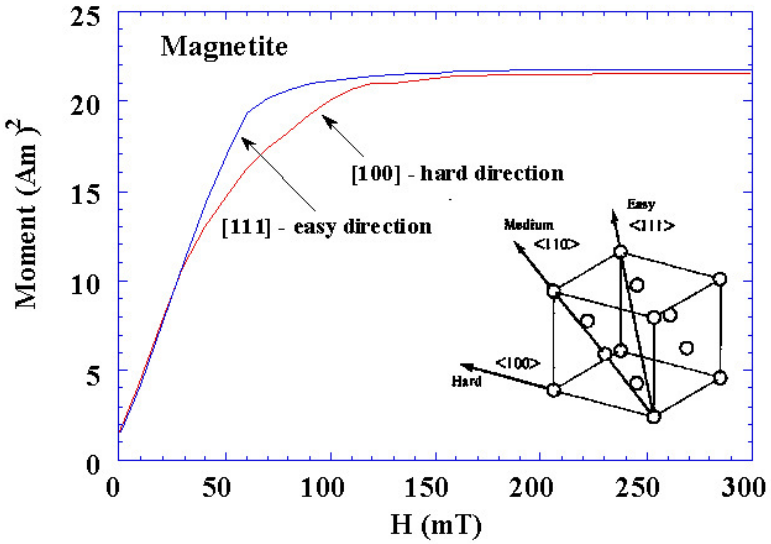

Figure 1.2: Magnetic curves of magnetite along $\langle 100 \rangle$ and $\langle 111 \rangle$ directions showing magnetic anisotropy between easy and hard axis. Taken from [9]

.

where ψ is an angle between external magnetic field and an easy axis and α_i is a directional cosine between magnetization and anisotropy axis and $K_{1c} = K1(sin^4\phi\cos^2\psi\sin^2\psi + \cos^2\phi\sin^2\psi)$

Shape anisotropy H_d is induced in non spherical samples due to non homogenious demagnetization field. This field creates one or more easy axes.

Induced anisotropy is created in the material if the easy axis is created by application of stress. Induced anisotropy may also occurs when depositing thin layer in magnetic field or when annealing disordered alloy due to creation of atomic scale texture due to atomic diffusion. The later is prone to happen in disordered alloys during annealing due to atomic diffusion [8].

1.1.3 Stoner-Wohlfarth model

Stoner-Wohlfarth (SW) model represents a simple phenomenological model for single domain FM magnetization modeling. Let us assume SW particle: An ellipsoid with uniform magnetization and uniaxial anisotropy (either magnetocrystalline or shape origin) in a magnetic field. Although originally intended for ferromagnetic materials the SW model can be used even for AFM materials. For FM the energy per unit volume divided by magnetization is equal to [10]

$$\frac{E}{MV} = -\vec{B}\vec{b} \cdot \vec{m} + B_a(\vec{m} \cdot \hat{a})^2 \tag{1.10}$$

where $\vec{b} = \vec{B}/B$, $\hat{a}$ direction of uniaxial anisotropy and B_a represent anisotropy field. In the case of AFM we assume to magnetization sub lattices with opposite direction of spins. The energy per unit volume divide by magnetization is given by [10]

$$\frac{E}{MV} = B_e\vec{m}_1 \cdot \vec{m}_2 - \vec{B}\vec{b} \cdot (\vec{m}_1 + \vec{m}_2) + B_a[(\vec{m}_1 \cdot \hat{a})^2 + (\vec{m}_2 \cdot \hat{a})^2] \tag{1.11}$$

Where B_e is an exchange term.

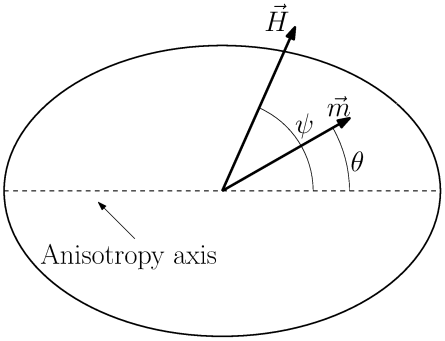

Figure 1.3: Stoner-Wohlfarth particle with denoted vectors of external magnetic field $\vec{H}$, its magnetization $\vec{m}$ and their respective angles ψ and ϕ.

If we define following angles ψ as an angle between the current dierction and the direction of the magnetic field and ϕ as an angle between the direction of the current and the direction of the magnetization $\vec{m}$ (or Néel vector) the previous equations reduces to almost similar form for both FM and AFM

$$\frac{E}{MV} = 2\alpha\cos(2\phi) - \frac{1}{2}\beta^n \sin^n(\phi - \psi) \tag{1.12}$$

where $\alpha = \frac{B_a}{B_e}$, $\beta = \frac{B}{B_e}$ and n = 1 for FM and n = 2 for AFM. Therefore the only difference between the FM and AFM case is the scaling with magnetic field B as the position of maxima and minima of the $\sin\phi$ and $\sin^2\phi$ are identical.

1.2 Electrical resistance

Based on its electrical transport properties we can divide materials into 3 basic groups. Insulators, semiconductors and conductors. Insulators do not contain any free charge carries due to their valence electrons occupying one or more energy bands while the other bands do remain empty. The band gap of insulators is usually of several eV (9 eV for SiO_2 [6]). The situation is similar for the semiconductors with the exception being lower band gap (1.12 eV for Si, 0.67 for Ge [7] [6] with room temperature resistivity of a non doped Si $\rho_{300}^{Si} = 2.3 \cdot 10^3\ \Omega{\cdot}m$ and the Ge resistance being $\rho_{300}^{Ge} = 4.6 \cdot 10^{-1}\ \Omega \cdot m$ [6]). Granting for excitation (thermal excitation, photo excitation, ...) of the electrons from the valence to the conductive band. Doped semiconductors have an extra energy levels due to dopant. Either in the vicinity of the valence band (p-type) or the conduction band (n-type) [6]. In the case of conductors the valence and conduction band overlap. This allow for two partially filled band and valence electrons are able to move freely within the conductive band.

In this thesis we will discus only the electrical conductors. Namely the electrical resistance of metals.

Electrical properties are usually described by a conductivity tensor $\overleftrightarrow{\sigma}$ which is defined by Ohm's law [7] [6].

$$\vec{j} = \overleftrightarrow{\sigma}\vec{E} \tag{1.13}$$

where $\vec{j}$ is current density and $\vec{E}$ is electric field.

In the scope of Fermi gas model [6] the conductivity tensor reduces to scalar, and can be written in a following form [7] [6]

$$\sigma = \frac{ne^2\tau}{m} \tag{1.14}$$

where n is number of electron in volume unit, e is a charge of electron, τ is a relaxation time (time between the collision of the electrons) and m is the mass of the electron. The resistivity is is then defined as

$$\rho = \frac{1}{\sigma} \tag{1.15}$$

During the experimental measurement we measure electrical resistance R. Resistance and resistivity are interlinked by following equation

$$R = \rho\frac{l}{S} \tag{1.16}$$

where l is the length of the sample and S is its cross-sectional area.

Sources of the electron scattering

Total electrical resistivity in metals is due to different sources of conduction electron scattering. The most common sources of electron scattering are following:

Impurities and defects: In ideal crystalline metal the zero temperature resistivity would drop to zero. However the crystallinity of real materials is almost never perfect due to various chemical impurities or static defects of the crystal lattice. Those defects represent a source of electron scattering which sums of to a temperature independent resistivity ρ_0.

The ratio between the room temperature resistivity ρ_{300} and the 0 K resistivity ρ_0 (obtained by extrapolating low temperature resistivity data to 0 K) is called Residual resistivity ratio (RRR) [6]

$$RRR = \frac{\rho_{300}}{\rho_0} \tag{1.17}$$

and serves as a rough indication for a purity and overall quality of the measured sample.

Phonons: The temperature dependence of resistance is governed mostly by a phonons and magnons. In the case of phonons, the source of electron scattering is due to collective excitation of the crystalline lattice. This resistivity addition can be expressed by a Bloch–Grüneisen formula [11]

$$\rho_p = A(\frac{T}{\Theta_R})^5 \int_0^{\Theta_R/T} \frac{t^5}{(e^t-1)(1-e^{-t})}dt \tag{1.18}$$

where A is a constant typical for a given metal, T is a thermodynamic temperature and Θ_R is a Bloch–Grüneisen temperature (approximately equal to Debye temperature) [6]. For a low temperature when $\Theta_R \gg T$ the formula can be aproximated to a $\rho_p \sim T^5$ dependence. While for a high temperatures $\rho_p \sim T$ holds.

Magnetic moments: Above the magnetic ordering temperature, i.e. in paramagnetic state the scattering on the disordered moment occurs. This addition to the resistivity ρ_{spd} can be written in form [11]

$$\rho_{spd} = \frac{3\pi m^*}{he^2 E_f} J_{ex}^2 (g-1)^2 J(J+1) \tag{1.19}$$

where $m*$ is effective mass of the electron, h is a Planck constant, e is a charge of the electron, E_f is Fermi energy, J_{ex} is interaction energy constant, g is Lande g-factor and J is total angular momentum. This addition is temperature independent.

When in ordered state, the scattering on magnons ρ_{mag} (collective excitation of spins) takes place instead of ρ_{spd}. The magnon contribution can be written in a form [11]

$$\rho_{mag} = AT^2 + BT(1 + 2\frac{T}{\Delta})e^{-\frac{\Delta}{T}} \tag{1.20}$$

where A, B and Δ are constant characteristic for a given material. At low temperatures the dependence of ρ_{mag} is quadratic in behavior. Therefore the scattering on impurities on phonons is dominant. The scattering on magnons is most prominent slightly below the ordering temperature.

Matthiesen's rule

It has been empirically observed that those individual scattering mechanisms, each with their own relaxation times, are independent and additive [6] with a total relaxation time τ which follows:

$$\frac{1}{\tau} = \frac{1}{\tau_1} + \frac{1}{\tau_2} + \frac{1}{\tau_3} + ... \tag{1.21}$$

where τ_1, τ_2, τ_3 are relaxation times of individual scattering mechanism. This empirical rule is known as Matthiesen's rule.

Employing the Matthiesen's rule and summing all of the scattering mechanism discussed above, we can rewrite eq. 1.21 into the following form:

$$\rho = \rho_0 + \rho_p + \rho_{spd} + \rho_{mag} \tag{1.22}$$

This behavior of resistivity is depicted in figure 1.4

It should be noted that more, complex phenomena such as electron-electron scattering, Kondo effect or weak localization which attributes to the total electrical resistance can occur in metallic system [7] [6]. Yet those are beyond the scope of this thesis.

1.2.1 Magnetoresistance

Magnetoresistance is defined by [8]

$$\frac{\Delta\rho}{\rho_0} = \frac{\rho(\mathbf{B}) - \rho(0)}{\rho(0)} \tag{1.23}$$

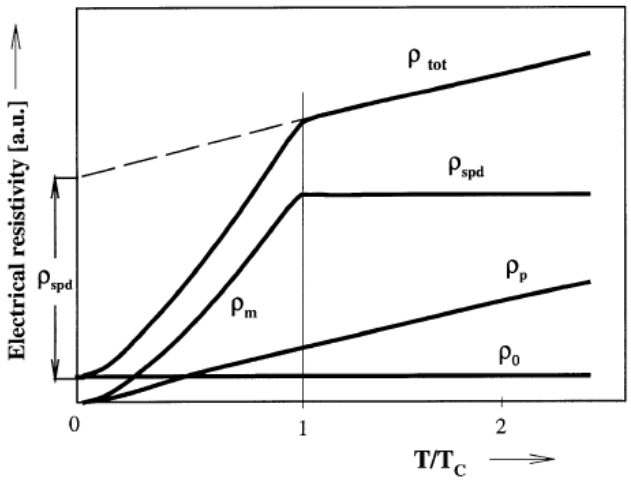

Figure 1.4: Graphical depiction of Matthiesen's rule. Taken from [12]

Motion of the electrons in the magnetic field for non magnetic metals can be explain withing the free electron model. From the equation of motion 1.24 [6], with a solution it can be seen that there is none longitudinal magnetoresistance

$$\hbar(\frac{d}{dt}+\frac{1}{\tau})\delta\mathbf{k} = -e(\mathbf{E}+\mathbf{v}\times\mathbf{B}) \tag{1.24}$$

$$v_x = -\frac{e\tau}{m}E_x - \omega_c\tau v_y \qquad v_x = -\frac{e\tau}{m}E_y + \omega_c\tau v_x \qquad v_x = -\frac{e\tau}{m}E_z \tag{1.25}$$

where $\hbar$ is reduced Planck constant and $\delta\mathbf{k}$ is shift of a k vector of Fermi sphere and $\omega_c = eB/mc$ is cyclotron frequency. Using the expression for conductivity (eq.1.14) we will obtain positive magnetoresistance $\Delta\rho \propto B^2$ [8] [6]. Expression for longitudinal magnetoresistance can be obtain by assuming two band model with electrons having different relaxation time τ and effective mass [8]. This yield again into the $\Delta\rho \propto B^2$ behavior [8].

1.2.2 Anisotropic Magnetoresistance

Anisotropic magnetoresistance (AMR) is dependence of resistivity on the angle between the electrical current and magnetization. It is defined as

$$\frac{\delta\rho}{\rho_\perp} = \frac{\rho_{||}-\rho_\perp}{\rho_\perp} \tag{1.26}$$

The angular dependence of saturated AMR (see fig. 1.5) is given by [8]

$$\rho(\varphi) = \rho_\perp + \rho_{||} - \rho_\perp cos^2(\varphi) \tag{1.27}$$

where φ is direction between the current density $\mathbf{j}$ and magnetization $\mathbf{M}$. The AMR is usually positive ($\rho_{||} > \rho_\perp$) due to spin-orbit interaction [8].

AMR can be explained within the two current Mott model. This model assumes that scattering of electron on impurities do not change its spin

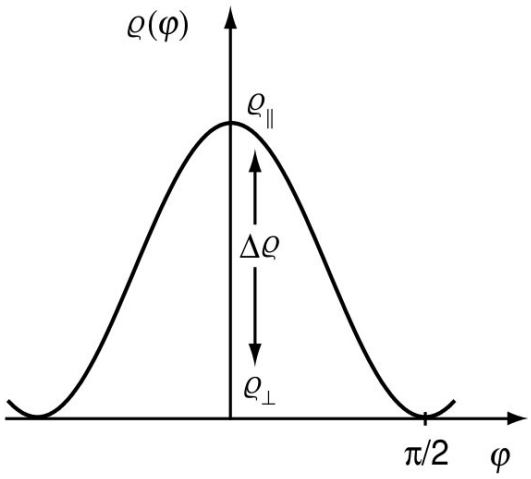

Figure 1.5: Angular dependece of AMR. Taken from [8]

orientation and the scattering differs for electron with spin ↑ and spin ↓. Then the total resistivity can be written in a form [13]

$$\frac{1}{\rho} = \frac{1}{\rho^{\uparrow}} + \frac{1}{\rho^{\downarrow}} \tag{1.28}$$

The spin mixing (due to magnon scattering) is introduced by a parameter $\rho^{\uparrow\downarrow}$ which represent the spin-flip transition. The total resistance can be rewritten in a form [13]:

$$\rho = \frac{\rho^{\uparrow}\rho^{\downarrow} + \rho^{\uparrow\downarrow}(\rho^{\uparrow} + \rho^{\downarrow})}{\rho^{\uparrow} + \rho^{\downarrow} + \rho^{\downarrow\uparrow}} \tag{1.29}$$

Different scattering rates occurs for electrical current parallel or perpendicular to the direction of magnetization. This is attributed to spin-orbit coupling. The AMR can be expresses by a following equation [13].

$$\frac{\Delta\rho}{\rho} = \gamma \frac{\rho_{\downarrow}(\rho\downarrow - \rho_{\uparrow})}{\rho_{\uparrow}\rho_{\downarrow} + \rho_{\uparrow\downarrow}(\rho\downarrow + \rho_{\uparrow})} \tag{1.30}$$

where γ describes the anisotropy of spin-resolved resistivities and is specified by a spin orbit-coupling [13].

If we assume that the AMR is dominated by non crystalline term:

$$\frac{\Delta\rho_{xx}(\phi)}{\rho_0} = Ccos(2\phi) \tag{1.31}$$

The angular sweeps in ψ can be simulated. Thanks to the relation between the ϕ and ψ provided by the SW model (eq. 1.12).

2. Experimental methods

This chapter gives an overview of an experimental methods and devices used during the work on this thesis. The most difficult part was the fabrication of device for electrical transport measurement. For the fabrication several advances methods including electron microscopy, focused ion beam milling and electron beam lithography were used.

2.1 Scanning electron microscopy

Scanning electron microscope is a device creating an image by scanning over the sample surface by a focused beam of electrons. The image is produced by collecting the particles produced by electron solid interaction.

Two scanning electron microscopes were used during the experiment: Mira I LMH and its newer version MIRA III LMH (fig. 2.1). Both of those are of similar construction. The main three parts are electron gun, column and chamber.

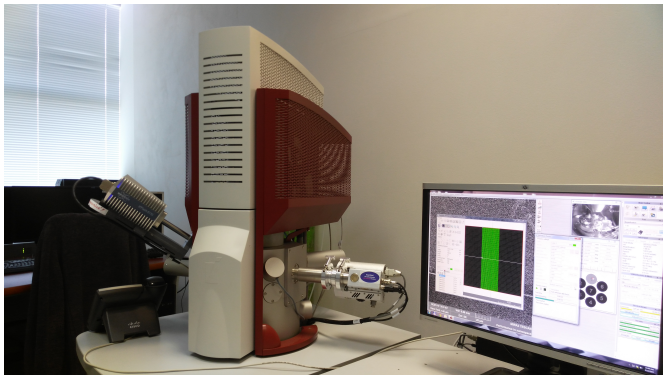

Figure 2.1: SEM MIRA 3

Electron gun is a source of electrons. In the case of SEM Mira I LMH and Mira III LMH the source is Schottky cathode. Schottky cathode is a tungsten wire formed into a shape of tip. It is coated by a thin layer of ZrO_2 which increases the electrical conductivity at high temperatures. Conventional electron sources (LaB_6, tungsten wire) uses thermal emission in order for the electron to overcome the potential barrier on the surface of the tip. Schottky cathode adds strong electrical field. This lowers the potential barrier and allows the cathode to work at lower temperatures of around 1800 ^oC [14]. Electron beam produced by Schottky cathode is, compared to thermal emission sources, smaller in diameter and is able to produce higher current densities. This results in higher spatial resolution and better signal to noise ratio. On the other hand, the price for the Schottky gun is higher compared to the ones of thermal emission and requires higher vacuum [14].

The electromagnetic lenses which are responsible for the focusation of the electrons into a narrow beam, are placed in **Column**. The electron current exiting from the electron gun is regulated by a condensor. Next the electron beam is focused into the axis of the column by a centering coil followed by apertures

lenses which are narrowing the beam down. Finally the scanning of the beam over the sample is done by scanning coils.

In the **chamber** detectors and samples are placed. Namely secondary electrons detector, backscattered electron detector and Energy-dispersive X-Ray spectroscopy detector.

2.1.1 Electron solid interaction

Interaction of primary electrons with solid matter is followed by a generation of particles and radiation. Namely secondary electrons (SE), backscattered electrons (BSE), Auger electrons and X-ray radiation. Such interaction is not strictly surface effect. The particles and radiation are also generated in a sample volume beneath the incident beam. The penetration depth of the incident beam depends on its energy and sample material.

Secondary electrons

During the collision of the primary electrons with the atoms of the material, the incident electron may kick out the electron out of the atomic shell of the material atoms. Those electrons are called secondary electrons (*SE*). As their mean free path in the material is usually few tens of nm [14]. Only those in a close vicinity of the surface are able to leave the sample. Their detection allow us to map topography of the sample. Energy of the secondary electron is usually in the range of units or tens of eV [14].

Back scattered electrons

Part of the incident electrons may elastically backscatter from the nuclei of the material. Those are called backscattered electrons (*BSE*). The probability of backscatter is higher for elements with higher atomic number Z. Hence in BSE contrast the areas of the materials which contains heavier elements do appear brighter, while the areas containing lighter elements appears darker.

Energy dispersive X-Ray spectroscopy

X-Ray radiation created with electron solid interaction has two parts. Characteristic radiation and Bremsstrahlung. The later is generated during the deceleration of the primary electrons due to their electrostatic interaction with the atoms of the matter. The change of the kinetic energy is converted into the radiations (fig. 2.2). The Bremsstrahlung has a continuous spectrum.

The characteristic radiations is created during the excitation of the electrons from the inner K or L shells from the atoms of the material. This unoccupied energy level is filled by an electron from an outer energy level. This is accompanied by a generation of a photon with an energy equal to the energy difference of those two energy level (see fig. 2.2). The spectrum characteristic radiation is discrete and is specific for each elements.

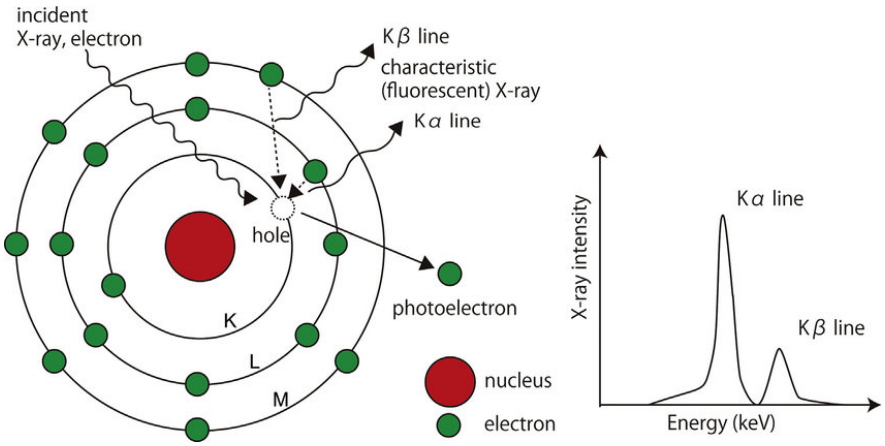

Figure 2.2: Simple scheme illustrating the creation of characteristic radiation Taken form [15].

Electron backscatter diffraction

In crystalline materials incidence of primary electrons on the sample surface can result in their diffraction by atomic layers. Detecting those diffracted electrons gives us direct information about crystal structure and orientation of the crystalline grain.

2.2 Focused ion beam milling

Since the release of the first commercial Focused Ion Beam (FIB) at the beginning of 1980s, [16] FIB found its steady place in semiconductor industry. However in the era where the research is more and more focused on the field of nanotechnology, FIB importance rises due to its versatility. Covering imaging, etching, deposition and manipulation on nanoscale level. More recently FIB has proven to be a useful tool when dealing with electrical transport properties of materials on micron scale level due to its precise control over the sample shape and geometry [17].

Working principle is similar to SEM but instead of using focused beam of electrons as a probe, ions are being used. Compared to electrons, mass of ions is several orders of magnitude higher. This allows FIB not only to work as a tool for imaging the sample surface like conventional SEM but also as a tool for etching or deposition.

Majority of commercially sold FIBs are coupled with SEM. So called dual-beam FIB-SEM. Usually the SEM column is perpendicular to the sample holder while the FIB column is tilted by a fixed angle (55 % in the case of used FIB Tescan Lyra I XMH - fig. 2.3) in respect to SEM. A simple scheme is depicted on fig. 2.4.

2.2.1 Construction of Focused Ion Beam

The most widely used source of ions is liquid metal ion source (LMIS) with gallium as typical metal being used. This is due to its low melting point (29.8 ^{o}C [18]) and non reactivity of the Ga with tungsten. Another advantage is that the

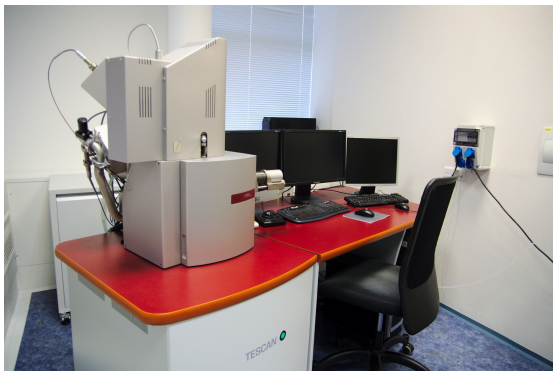

Figure 2.3: FIB Tescan LYRA XMH.

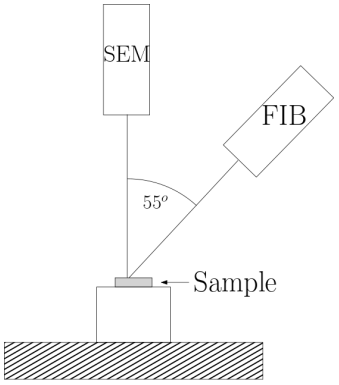

Figure 2.4: Simple scheme of FIB-SEM dual beam geomtry.

mass of Ga ions is high enough so that they can etch even the atoms of heavier elements from the sample.

The reservoir of metal is heated above its melting point and the liquid is let to run down the tungsten wire with a 2-5 μm tip. By the application of strong electric field, created by and electrode called extractor, (voltage is typically 6-8 kV) an emission of positive ion is generated from a liquid cone (called Taylor cone). The cone is formed on the tungsten tip due to equilibrium of surface tension and electrostatic force. The ion current is then regulated by another electrode of opposite voltage called supressor further into the ion column.

When the beam of ions enters the column it is formed by a strong electromagnetic lens called condensor and focused on a sample surface by means of objective lens. Additional modification as an ion beam current change (ion current are typically from few pA to 30 nA) and its spot size on a sample surface is governed by a set of apertures of different sizes. The typical ion current are ranging from few pA, which are suitable for high resolution imaging, up to $\sim$ 30 nA used for fast and rough milling. The astigmatism and the scanning of the beam over the sample is set up by a set of octupole lenses. In order for the ion optics to work properly and the emission of ions to be stable a high vacuum of 10^{-7} Pa has to be maintained in the column.

2.2.2 Ion solid interaction

In order to understand FIB imaging, etching and deposition abilities we must look into how the incident, highly energetic ions, interact with solid matter.

Imagining

During the collision of the ions with matter, the ions loose their energy due to the interaction with electrons and nuclei. The collisions of the ions with the electrons are inelastic and the energy losses of the incident ions are negligible. Result of this interaction is either emission of the X-Ray radiation or excitation of the electron from the atomic shells. Collecting those secondary electrons by a positive voltage electrode allows for imagining of the sample surface.

Milling

Most of the initial momentum of the incident ion is given to the nucleus.This often leads to the displacement of the atoms or the sputtering of the atoms from the sample surface. This effect is behind the FIB ability to mill.

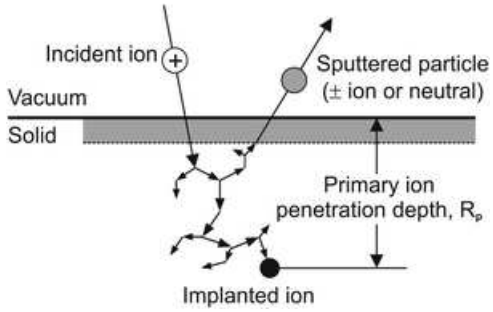

Figure 2.5: Scheme of ion solid interaction. Taken from [19]

Redeposition

During the milling, some of the atoms which are supposed to leave the sample, are adsorbed back into the milling area. This effect is dependent on material, geometry of the milled structure and way of scanning. Is is possible to reduce this effect with repeated scanning of the beam over the area. It was shown that the redeposited layer contains higher amount of Ga [20].

Surface damage

The atom which was displaced by the incident ion may also give its momentum to another atom in the solid and so on, leading to creation of cascade. Those displacement cascades are more prominent if the mass of the incident ion is comparable or higher than the mass of the atoms in solid. This leads to the implantation of Ga ions into the material and amorphization of the surface.

The mean free path of the ions, which are accelerated up to 30 kV (typical acceleration voltage in FIB), is typically tens of nm [17]. This has been routinely observed in FIB prepared Transmission Electron Microscope (TEM) lamellae. In TEM, we can usually observe an intact crystalline core sharply separated by a thin Ga rich (5-10%) amorphous layer of a typical thickness 10-20 nm [16]. In regards to FIB microstructuring of a transport devices the Ga rich amorphous layer can present significant contribution to a total device resistivity in case of insulators or semiconductors. However in case of metals, the contribution from a disordered amorphous layer should be negligible from a point of view of parallel resistors. This is indeed confirmed by numerous studies showing good agreement between transport properties of bulk material and FIB device [21] [22] [23] [24]. In addition, quantum oscillations were often observed in FIB transport devices giving further evidence of an intact crystalline core [22] [23].

Deposition overspray

Deposition by IA-CVD is often accompanied by a deposition outside the targeted deposition area due to generation of highly reactive, only partially decomposed

precursor molecules [23]. This effect is called halo or overspray [17]. Even though conductivity of this overspray is less conductive than the original deposit, it may still cause current leakage. The current leakage is behind the failure of your previous work [25]

2.2.3 Gas injection system

One of the most crucial capabilities of FIB systems is to locally deposit different type of materials like insulators and metals on nano scale. With the most common being platinum, tungsten, carbon and silicon dioxide. This is called ion assisted chemical vapor deposition (IA-CVD) and is achieved by a so called Gas Injection System (GIS) (fig . 2.6).

Volatile precursor in the form of gas is injected by a nozzles into a vicinity of the targeted area. This precursor is then decomposed via focused ion beam into volatile and non volatile components. Non volatile components are adsorbed on a sample surfaced while the volatile ones are vented away by a vacuum system. The deposition rate is influenced by many factors: The distance of the nozzles from the substrate, the ion beam current, the dwell time (time for which ion beam stays on one pixel) or the overlap of the beam spots. Those parameters have to be tuned before every deposition in order to deposit quickly and to obtain high quality layer.

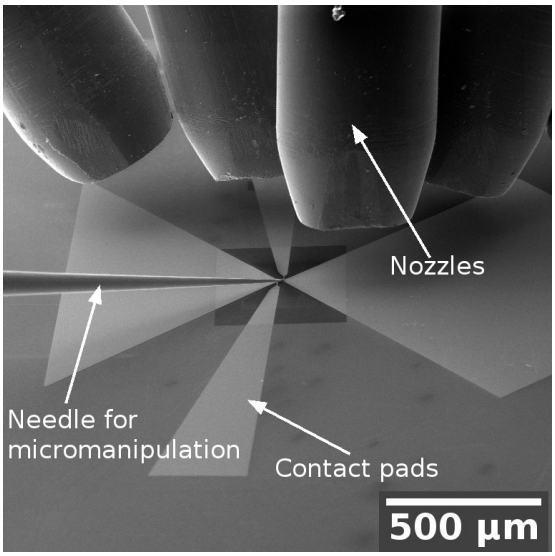

Figure 2.6: Gas injection nozzles as seen by SEM

The speed of the deposition is determined by the position of the nozzles and ion beam current. However with higher ion fluxes, the "milling" part of FIB starts to get upper hand on the "deposition" part. It is therefore necessary to change either dwell time - to reduce the ion dose (number of incident ions per cm^2) or change beam overlap [16].

2.3 Electron beam lithography

Various lithography techniques are being used nowadays. Amongst them photolithography takes a prominent place due to its usage in semiconductor

industry where its used to fabricate complex integrate circuits due to its speed and recently due to development its resolution. Photolithography requires lithograph and physical mask. Both are costly.

Electron beam lithography (EBL) is slower, but it does not require physical mask. The resolution is higher ($\sim$ 10 nm) [26] and it is possible to do the exposition on a slightly modified SEM. Those reasons makes EBL more common in basic research where the SEM modification (beam blanker is needed to deflect the electron beam) is less expensive than buying a lithograph. No need for physical mask allows for a wide variety of structures and the low speed doesn't represent a big problem due to low amount of created structures. This is also our case as Tescan Mira 3 LMH is equipped with beam blanker and software for lithography Draw Beam by Tescan. EBL process consist of several steps: Application of resist on substrate, exposition of resist by electron beam, removal of exposed part (development), sputtering of a functional layer and finally removing redundant function layer (lift-off). Those steps are graphically represented in fig. 2.7 and further discussed below.

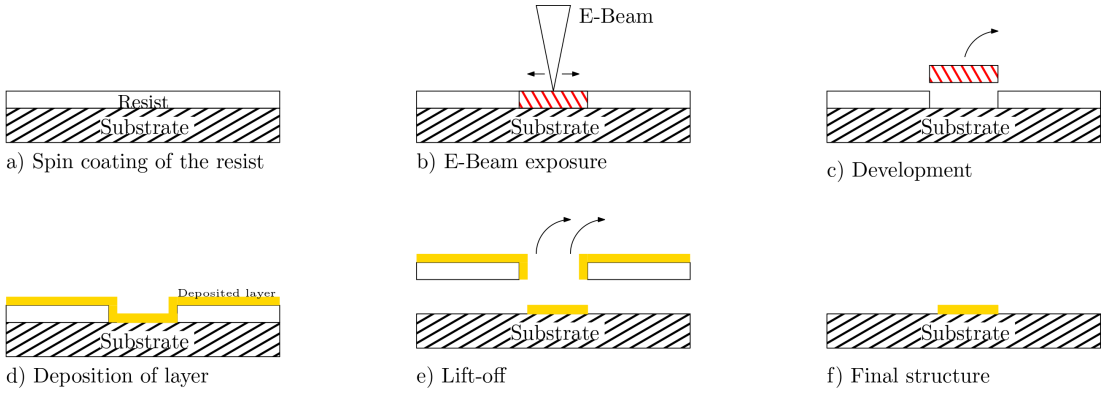

Figure 2.7: Graphical scheme of EBL steps

Application of resist

E-Beam resist are chemical substances which are sensitive to the electron beam irradiation. Typically these are polymers dissolved in organic solvent whose structure undergo a significant change due to exposure. Those exposed part are then easier/harder to remove. If the exposed parts are easier to remove then we talk about positive resist. When its opposite we speak of negative resist. In the positive resist, long molecular chains are shortened by e-beam exposure. This is called chain scission. Most common and widely used positive resist is PMMA, while the others being Accuglas, EBR-9, PBS or ZEP [26]. On the contrary, molecular chain of negative resist are cross-linked together into a longer chain which makes them harder to remove. We may name COP, Calixaren [26] or over exposed PMMA as a typical representative of this group. Application of the resist on the substrate is typically done via spin coat method. Drops of E-Beam resist are sprinkled across the substrate and by spinning the substrate, homogeneous layer is created. Further baking of the substrate with the resist on a hot plate allows for evaporation of organic solvent and better adhesion of the layer. When the substrate is insulator the substrate has to be coated by a thin

conductive layer so that the structure won't get distorted due to charging. The layer has to be sufficiently thick so that the charge would be carried away but also thin enough as the electron beam has to pass through. Material of the coating layer has to be easy to remove. Usually 5 nm of Cu is used.

Exposition

Exposition is determined by several parameters which needs to be tuned for different types and thicknesses of the resist. Namely Dose D which is defined as an electric charge hitting a unit surface area, beam step size d_{bss} representing distance between 2 pixels, dwell time t_{dwell} which is a time for which a beam stay on one pixel and beam current I. Those parameters are interlinked by following formula [26]

$$t_{dwell}(s) = \frac{D(\frac{\mu C}{cm^2}) \cdot d_{bss}^2(\mu m)}{0.1 I(nA)} \tag{2.1}$$

Proximity effect Irradiation of the resist may lead to exposure of parts of the resist which were not supposed to be exposed. This effect, called proximity effect is particularly prominent during the exposure of two nearby structure. Several contributions adds to this effect.

Backward scattering Collision of the primary electrons with the atoms of the substrate may lead to their scattering under high angle back into the resist which leads to exposure of the previously unexposed area.

Forward scattering On the other hand forward scattering is caused by a small angle scattering from the molecules of resist. Which results in effective enlargement of the electron beam on the bottom of the resist. This effective enlargement d_f depends on the thickness of the resist R_t and the high voltage of the electron beam V_h can be described by an empiric formula [26]

$$d_f = 0.9 \left(\frac{R_t(\mathrm{nm})}{V_h(\mathrm{kV})} \right)^{3/2} \tag{2.2}$$

As can be seen from eq. 2.2 using thinner resist and higher voltages leads to lowering of forward scattering.

Secondary electrons Secondary electrons which are created during the collision of the primary electrons with the atoms of the resist may also contribute to and effective broadening of the exposed parts. Nonetheless as the energy of the secondary electron is relatively low, (2-50 eV) their mean free path in the resist is short. Thus lateral broadening of the beam is only few nm [26].

Development

Removal of the exposed parts is done by submerging the substrate into a developer. This process is called development and is dependent on the type of the resist and its thickness. After the removal of the substrate with the resist from the developer, substrate has to be submerged into a stopper and then

dried. For widely used resist PMMA there is possibility to use several developers. Namely MIBK/IPA in the ratio 1:3 or IPA/H_2O in the ratio 3:7 [26]. As a stopper IPA is used.

Deposition of functional layer

Many deposition techniques are being used nowadays with most common ones being sputtering and evaporation.

Magnetron Sputtering During the sputtering process atoms of the sputtered material (target) are deposited on the substrate. Target is connected to an anode with a strong magnets in its vicinity. The substrate is connected as a cathode. Chamber with target and substrate is filled with inert gas (usually argon). By increasing electric potential between those two electrodes, secondary electrons starts to emit from the cathode which leads to ionization of the inert glass. This effect is further amplified by a magnetic field. Ions attracted to a cathode starts starts to bombard the target. Atoms of the target are ejected during the collision and they start to deposit on the substrate. The trajectory of the atoms is non directional. This leads to deposition to a surfaces (see fig. 2.8) which are in the geometrical shadow. For example side walls of the resist and substrate

Thickness of the layer is usually measured using quartz crystal method (QCM). This method measures change of the resonance frequency of quartz crystal with its changing mass due to deposition of the material on its surface.

Evaporation Source material is placed in a crucible where it is heated by electrical filament. As the process takes places in a high vacuum, mean free path of the evaporated source atoms is long enough so that they may condensate on the substrate. Apart from sputtering deposition by evaporation is single directional (see fig. 2.9). As the resist walls are not sputtered, evaporated layers have better resolution and their lift-off is easier.

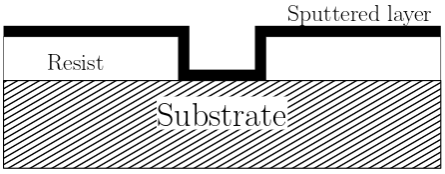

Figure 2.8: Cross section of thin layer prepared by sputtering.

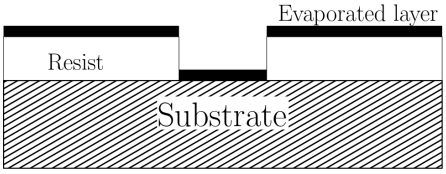

Figure 2.9: Cross section of thin layer prepared by evaporation.

Lift-off

Last step of EBL is removal of the resist so that only the functional layers in the exposed parts remain. Substrate with resist is submerged into a solvent which is characteristic for each resist. Time for which the substrate has to be submerged differs for different resists and different thicknesses from couple of minutes to several hours. This process can be hurried by using ultrasound cleaner, however it may remove the functional layer from the substrate when the adhesion is not good. After the removal of the resist it is recommended to wash the substrate

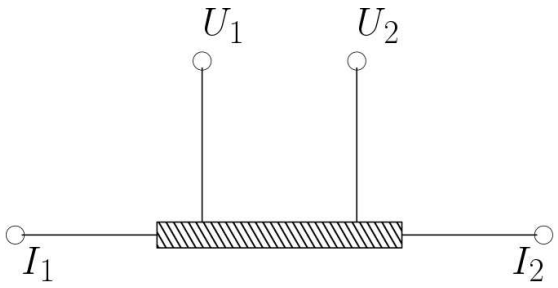

Figure 2.10: Scheme of a four point probe method. Taken from [25]

in the developer to remove potential residue of the resist. For PMMA, acetone is widely used as an remover where it is left for approximately hour so that the remover could get to all parts of the resist. In the case of thicker functional layer (t $\geq$ 200 nm) and large structure it is possible to remove the layer by using a tweezer.

2.4 Electrical resistivity measurement

Electrical transport properties were measured by Physical Properties Measurement System (PPMS) by Quantum design. This system allows for measurement of wide variety of physical properties in wide temperature range 1.8 - 400 K and in magnetic fields up to 9 T (14 T in case of 14 T PPMS).

Resistivity measurement is ensured by an alternative current transport (ACT) option. This option supplying currents up to 2 A via source in a frequency range 1 Hz - 1 kHz. Measurement itself is done by a four point method.

Four point probe method is suitable for measuring small resistances. Typically rectangular sample is contacted by a four wires as is depicted in fig 2.10. Two wires I_1 and I_2 are used to inject the current through the sample. Wires U_1 and U_2 are voltage contacts. Advantage of this method is that the resistance of the sample is of orders of magnitudes lower then the resistance of the wires and the internal resistance of voltmeter. Therefore it is safe to assume that the resistance of the contacts and attached wires is negligible and we are measuring only the voltage drop across the sample.

ACT option requires contacting the sample in a special holder (puck) made by *Quantum Design*. This allows for measuring up to 2 sample via four point method. Contact are usually done by a connection of a thin metallic wire (Cu, Au, Ag) with a sample by a silver epoxy paste.

3. The physical properties of CuMnAs

Thin layers

The tetragonal CuMnAs in the form of thin films have been studied since 2013 [27] due to its promising application in AFM spintronics. CuMnAs is grown by molecular beam epitaxy on either GaAs(001) (relaxed) or GaP(001) (fully strained). The space group was found to be the one of tetragonal Cu_2Sb type structur(e *P4/nmm*) (fig. 3.1) with a lattice parameters $a = b = 3.820$ Å, $c = 6.318$ Å[27].

In regards to magnetic properties, tetragonal CuMnAs orders antiferromagnetically with Néel temperature $T_N = 480$ K. Its magnetic structure is collinear with a propagation vector $\boldsymbol{k} = (0\ 0\ 0)$ [28]. On the other hand, the direction of the spins is not entirely clear. Studies on 500 nm thick film [28] suggests biaxial magnetocrystalline anisotropy with spins pointing either along <1 0 0> or
<1 1 0> direction. The precise determination is complicated due to presence of magnetic domains with equal projection of spins pointing along [1 0 0] and [0 1 0] [28]. However for the 10 nm thick films the situation differs. It appears that the uniaxial magnetocrystalline anisotropy is present with the spins pointing along <1 0 0> direction [28]. This is believed to be interface effect [29], [28] and it is not a bulk property as such.

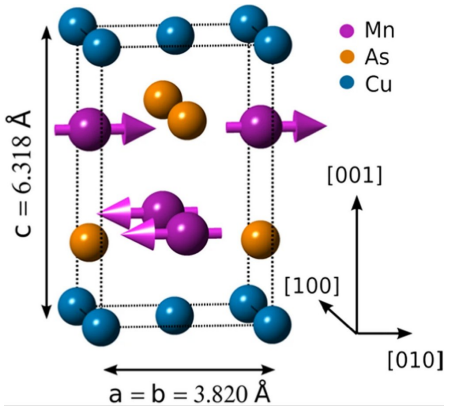

Figure 3.1: Structure of a thin layer tetragonal CuMnAs grown and its magnetic structure . Taken from [28].

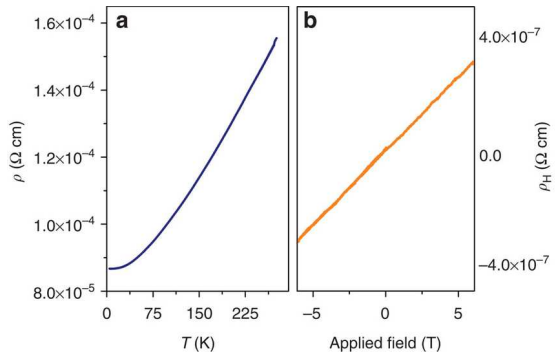

Figure 3.2: Temperature dependence of resistivity (along [0 0 1]) of CuMnAs thin layer and Hall resistivity as a function of a magnetic field. Taken from [27].

The main focus, however has been on electrical transport properties. Especially the selective manipulation of magnetic moment via electric current by a means of spin-orbit torque [30]. This allows for an effective writing of the information. The reading, although little explored, is done by a means of AMR. This gives different reading signals for two perpendicular orientations of magnetic moments.

Since the limitations of the epitaxially grown thin layer, the temperature

dependence on resistivity has been measured only in a [0 0 1] direction [27] (see fig. 3.2). Due to the layered structure of CuMnAs an anisotropy between both principal crystallographic directions is expected.

Bulk

In the bulk form the situation differs. Originally CuMnAs was believed to crystallize in an orthorombic form (*Pnma*) [3] [4]. Recent studies has shown that different kinds of structures of Cu-Mn-As system are stabilized as the composition vary (see fig. 3.3 and [31]).

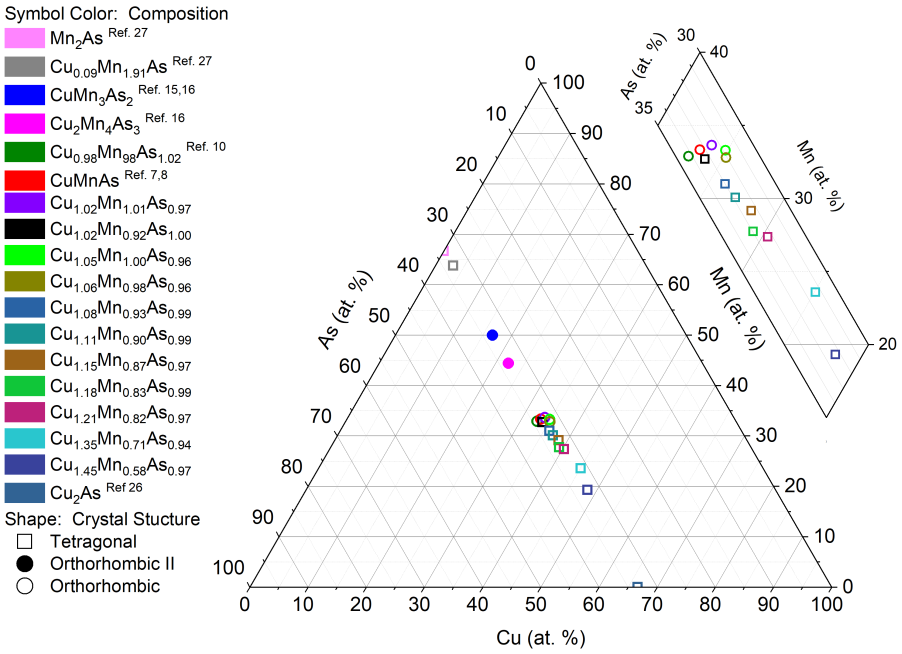

Figure 3.3: Ternary diagram of Cu-Mn-As system. Taken from [5].

The orthorombic I (space group *Pnma*) structure is stabilized when the stoichiometry is 1-1-1. This orthombic modification has has been proposed as a first Dirac material with magnetic ordering [32] and has been studied both experimentally and theoretically [3] [33] [34]. Excess of the Mn ($Cu_2Mn_4As_3$, $CuMn_3As_2$) leads to a stabilization of Orthorombic II (space group *Pnma*) structure which is doubled along a axis compared to the Orthorombic I [31] [35]. Lately it has been reported that the hexagonal structure (space group $P\bar{6}$) is formed for the composition $Cu_{0.82}Mn_{1.18}As$ [36].

Tetragonal modification (space group P4/nmm) is formed in As and/or Cu rich samples with Mn deficiency [5]. The lattice parameters are in an agreement with a thin layers grown on GaAs(001) [27], suggesting that the thin layers are also Mn deficient. The Néel temperature of the nearly stoichiometric tetragonal $Cu_{1.02}Mn_{0.99}As_{0.99}$ is $T_N = 507$ K [5] and it decreases with increasing amount of Cu. First studies of the charge transport properties of the bulk tetragonal

CuMnAs are subject of this thesis and have been recently reported in our paper [10]

4. Sample preparation

4.1 Sample preparation and characterization

In this work sample from our previous study [5] was used. We choose the composition closest to the CuMnAs 1-1-1 stoichiometry and still has the tetragonal symmetry (slightly Cu rich). Polycrystalline samples of tetragonal CuMnAs was grown by a direct synthesis of high purity Cu, Mn and As in a 1.000:0.964:1.036 molar ratio as reported in [5]. The weighted elements were placed in an alumina crucible and sealed in quartz ampules under 0.2 Bar of Ag. The sample was heated with a ramp of 0.1 ^{o}C to 1090 ^{o}C (24 h) and then cooled down to 980 ^{o}C (7 days) in order to improve homogenity.

The composition of the polycrystalline sample was checked by SEM EDX with a resulting stoichiometry $Cu_{1.02}Mn_{0.99}As_{0.99}$. This slight excess of Cu and deficit on Mn is sufficient for stabilizing the tetragonal structure with the the space group P4/nmm [5]. This was confirmed by a powder X-Ray diffraction [5] performed on a small piece taken from the polycrystalline sample. In a further text we will mostly refer to the $Cu_{1.02}Mn_{0.99}As_{0.99}$ as tetragonal CuMnAs as this was the only sample composition used.

A single crystalline grain ($\sim$ 0.4 mg) was chipped out of a polycrystalline sample. Its tetragonal structure with space group P4/nmm was confirmed by single crystal XRD (fig . 4.2). Further more its orientation was determined as shown in fig. 4.1

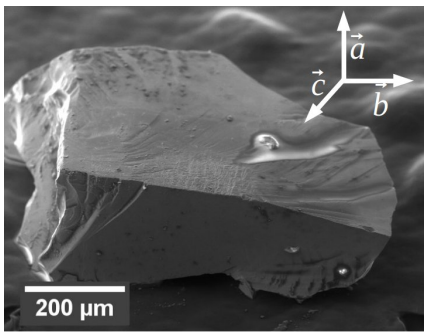

Figure 4.1: Single crystal grain of CuMnAs used for magnetization measurement and FIB microfabrication. Its orientation is represented by the axes in the top right corner.

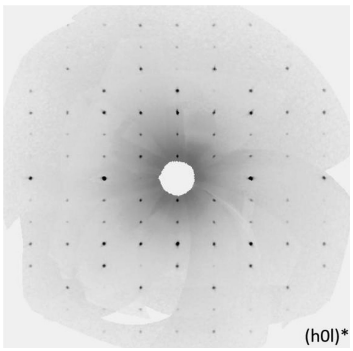

Figure 4.2: Single crystal XRD pattern of the tetragonal CuMnAs single crystal presented in fig. 4.1. Taken from [5]

4.2 Sample fabrication

We aimed to measure electrical transport properties of tetragonal CuMnAs including precise values of resistivity along both principal crystallographic directions. This require precise control over sample orientation and determination of sample dimensions. Unfortunately the only available sample

had sub millimeter dimensions and irregular shape, excluding the traditional methods for transport measurement. Therefore we decide to employ a sample fabrication method using FIB [21]. Such charge transport device fabrication comprises of two steps. Preparation of macroscopic structures with contacts pads and fabrication of microscopic sample.

The process of microfabrication was discussed in my bachelor thesis [25]. However the resistance of the previously microfabricated devices didn't correspond to the one of the original bulk. This behavior was clarified after the submission of the bachelor thesis. During the GIS deposition of Pt some of the overspray got underneath the sample which created current leakage [37]. In order to avoid this leakage a new method of microfabrication was adopted [21]. This process consist of several steps and will be described in details bellow.

4.2.1 Contact pads fabrication

Electrical connection between the microscopical sample and macroscopic sample holder is achieved by a contacts pads prepared by e-beam lithography (Tescan MIRA III).

Contact pads were fabricated on a 5x5x0.5 mm^3 sapphire substrate. Prior to the coating of the substrate with resist, the substrates were cleaned in an acetone and IPA. Then the first layer of PMMA resist Allresist ARP 662.06 600K (anisol) was spin coated at a 4000 RPM followed by a bake on a hot plate at 180 ^oC for 5 min. The procedure was repeated with the second layer of less sensitive PMMA resist Allresist ARP 662.06 600K (anisol).

Due to insulating properties of sapphire a 5 nm of Cu was deposited on top of the resist by magnetron sputtering (Quorum Technologies Q300TD). Electron beam of 20 keV and ion current of $\sim$ 4800 nA was used during the exposition. The dose used for this resists was determined in bachelor thesis [25] as a dose $D = 350\ \frac{\mu C}{cm^2}$.

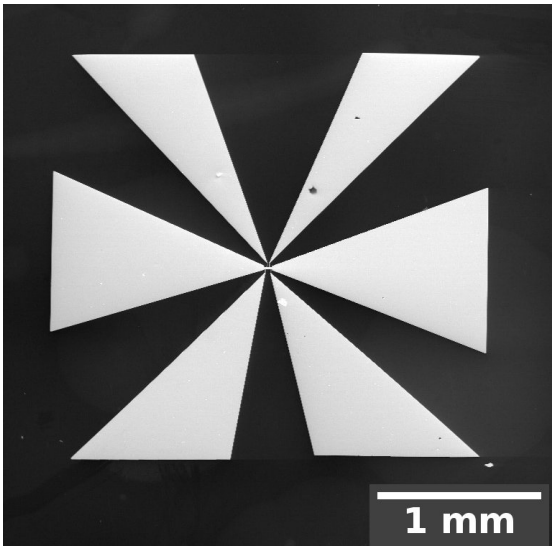

Figure 4.3: SEM micrograph of fabricated contact pads. This contact design allows for measurement of two resistivity channels using four point probe method using the same current electrical contacts.

Prior to the development the substrates were dipped into a diluted (10 %) HCl to remove the thin Cu film from the top of the resist. Then quickly put into the purified water to remove the traces of the acid from the substrates and dried by nitrogen. The mixture of IPA and purified water in the ratio 1:3 was used as a developer. Exposed substrates were submerged in the developer for 45 s [25] and dried by nitrogen.

Functional layer in the form of bilayer Cr(5 nm) + Au (150 nm) was deposited by evaporation (Angstrom Covap). The thin layer of chromium is deposited on the substrate due to bad adhesion of gold on sapphire.

During the lift-off process the substrates were submerged into a warm acetone for approximately 1 hour. While still in the acetone the excess layer of gold was removed by tweezer. In order to remove the resist and gold residues the substrates were put into the ultrasound cleaner for 30 s. Finally the substrates were cleaned by IPA to remove any acetone residues and dried by nitrogen. The final contact pad is to be seen in fig. 4.3.

4.2.2 Lamella fabrication

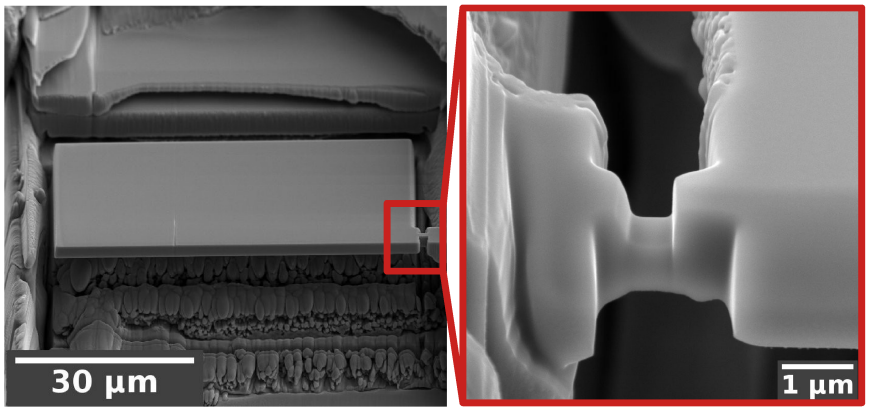

Figure 4.4: Lamella prepared for transport with a detail of the bridge holding the lamella with the rest of the crystal

Pre-oriented single crystalline grain of CuMnAs (see fig. 4.1) was attached on a wedge SEM holder by a conductive tape (we use 20^o wedge shape holders due to the FIB geometry. For more details see [25]) and subsequently put into the FIB Tescan Lyra I XMH. By using high ion currents ($\sim$ 16 nA, 30 keV) a rectangular plate (ac plane) of dimensions $\sim$ 70x8 μm^2 was carved into the single crystalline grain . The sample was then rotated by a 90 degrees so that the plate could be undercuted (see fig. 4.4) forming a lamella of dimensions $\sim$ 60x20x8 μm^3 hanging on a small bridge in one of its corner fig. 4.4). Lamella was then polished with a lower ion current (better focusation of the ion beam) of $\sim$ 4 nA under a grazing

angle of 3 degrees from each side to compensate for the effect of redeposition. The thickness after this polishing was about ~ 4 μm. The rectangular plate was then polished, again under a grazing angle of 3 degrees, by a small ion current ($\sim$ 400 pA) to cut down any potential surface damage layer caused by high ion currents resulting in a lamella of dimensions $\sim$ 60x20x3 μm^3. Finally the thin piece of material holding the lamella was narrowed down to a small bridge of dimension $\sim$ 0.5 x 0.5 x 0.5 μm^3.

Lamella transport

Single crystal grain (still attached on the SEM holder) with the lamella holding on a small bridge was removed out of a FIB and put under the optical microscope equipped with micro manipulators. A kapton crystalographic needle (MiTeGen Dual Thickness MicroMounts 10 μm) was mounted into the micro manipulator. Approaching and slowly crashing into the lamella results in a breaking of the thin bridge holding the lamella and attaching of the lamella to the kapton needle due to electrostatic force (see fig. 4.5). The kapton needle with the attached lamella is brought near to the sapphire substrate with a prefabricated contact pads. The lamella is dropped onto the substrate where it sticks by an electrostatic force (fig. 4.6). The lamella has to be well polished otherwise a gap between the lamella and substrate will be formed, which may result in adhesion problems. This result in an irretrievable loss of the prepared lamella as demonstrated in fig. 4.6.

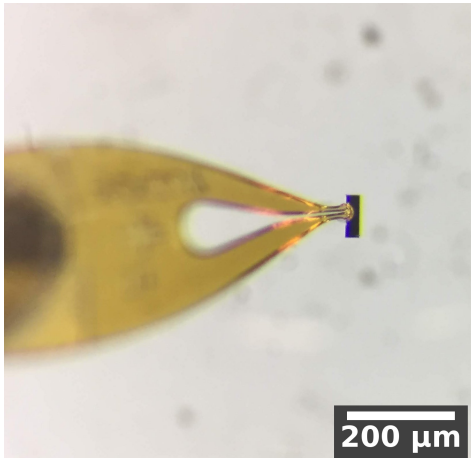

Figure 4.5: Micrograph of a lamella attached to a crystallographic needle

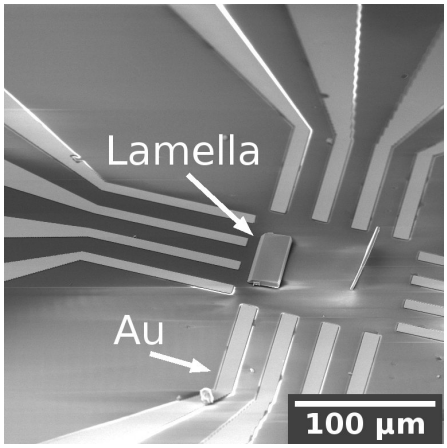

Figure 4.6: Lamella which has been dropped on a contact pads. Note the bad adhered lammela on the right

Final microfabrication

When the lamella is well placed on the substrate, the substrate is then attached to a SEM holder and inserted back into the FIB microscope. In order to conductively connect the prefabricated contact pads on the substrate with the lamella a GIS Pt deposition were used. Typical resistance of each contact prepared this way is around 50-100 Ω depending on the thickness of the deposited Pt layer and its length. In order to avoid any current leakage which could be potentially caused by a Pt overspray a thin and shallow trenches (width $\sim$ 5 μm, depth $\sim$ 2 μ m)

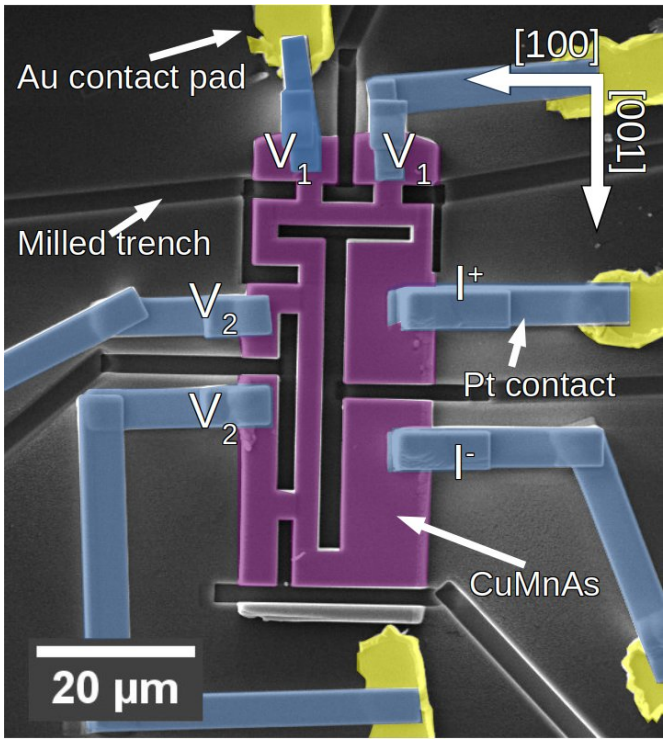

Figure 4.7: Microfabricated sample of CuMnAs. The I^+ and I^- contact are for injecting the current, the V_1 and V_2 are for measuring the voltage drop. The contact pads are colored in yellow, the Pt contact are blue while the sample is purple. Modified picture from [10].

were milled away between each contacts. Subsequently a thin surface layer (depth ~ 0.2 μ m) was removed from the top of the lamella by a low ion current of $\sim$ 200 nA to further remove any stray Pt overspray. Finally the desired shaped was cut into the lamella by using ion current of $\sim$ 400 pA. The final shape consist of two connected perpendicular narrow beams, allowing for electrical resistance measurement along a axis (10x3x3 μ^3) and c axis (20x3x3 μ^3) by a four point method. See 4.7 for more details. Depending on the lamella size fabrication of such sample may take between 15-30 hours.

In total 3 samples of same shape and similar dimension were fabricated to check for the reproducibility of the results. In the case of the Sample 1 the orientation of single crystal grain was done exclusively by single crystal diffraction and then attached to a SEM holder. Resulting in a slight misorientation of the Sample 1. In later cases of Sample 2 and Sample 3 the orientation of the grain on the SEM holder was further refined by EBSD. Fonfirming a misorientation of Sample 1 by about 10^o. The effect of the orientation on the resistance will be discussed later on.

5. Results and discussion

5.1 Magnetization measurement of polycrystalline and single crystalline tetragonal $Cu_{1.02}Mn_{0.99}As_{0.99}$

polycrystalline CuMnAs

A piece of polycrystalline sample (69 mg) was powderized and its magnetic properties were measured by PPMS using vibration sample magnetometer (VSM) option. Temperature dependence of magnetization in a field of 1 T is shown in fig. 5.1.

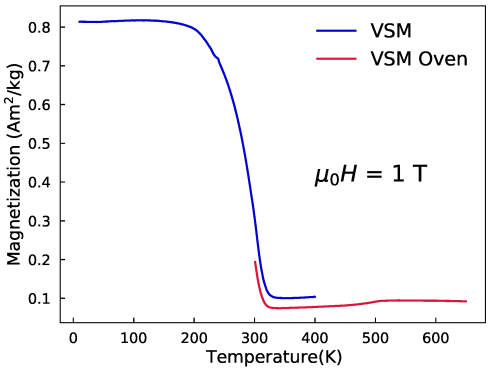

Figure 5.1: Temperature dependance of magnetization in a field 1 T. The sample had to be removed in between the high temperature measurement (red curve) and low temperature measurement (blue curve.)

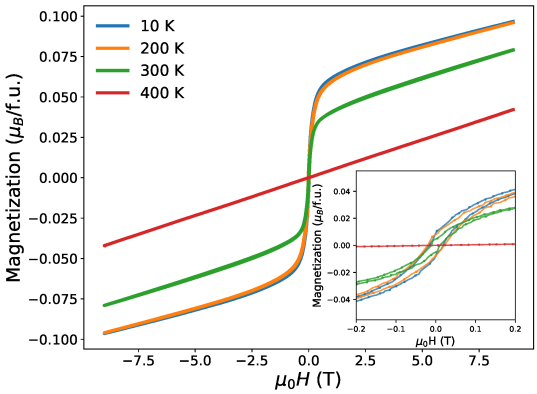

Figure 5.2: Magnetization curves at various temperatures of polycrystalline CuMnAs. A weak impurity-based FM signal from can bee seen at 300, 200 and 10 K.

The sample shows AFM transition at T_N = 507 K which correspond to the previously reported value [5]. Furthermore it also exhibits FM transition at T_C $\sim$ 320 K. This behavior is further visible on magnetization curves at different temperatures as shown in fig 5.2. At 400 K when the sample is above the FM transition, we can observe linear response of the magnetization up to fields of 9 T. When bellow the FM transition i.e. 320 K, the magnetization curve exhibits hysteresis behavior typical for FM. This FM behavior is not an intrinsic property of the bulk tetragonal CuMnAs. Rather it is presumed to be of MnAs impurity [5] due to its corresponding Curie temperature T_C = 320 K. [38]. From the magnetic signal the amount of MnAs impurity is estimated to be between 1.5 - 2 %.

Magnetization measurement of single crystalline CuMnAs

In order to verify that the FM signal came from an impurity presented in the polycrystalline sample rather than being intrinsic, the well characterized single

crystalline grain presented in fig. 4.1 was subjected to a magnetization measurement as well.

$Cu_{1.02}Mn_{0.99}As_{0.99}$ single crystal tetragonal structure with the space group *P4/nmm* was confirmed by single crystal XRD. Further more its orientation was determined as shown in fig. 4.1

The low sample mass ($\sim$ 0.4 mg) did not allow for a high temperature VSM (VSM with an oven) measurement due to the worse background caused by a holder. Therefore the magnetization measurement was measured by MPMS 7 (SQUID) only up to 400 K. Temperature dependance of magnetization in the temperature range 2 - 400 K in the magnetic field of 1 T along the [001] direction and magnetic field dependence at various temperatures are plotted in fig. 5.3.

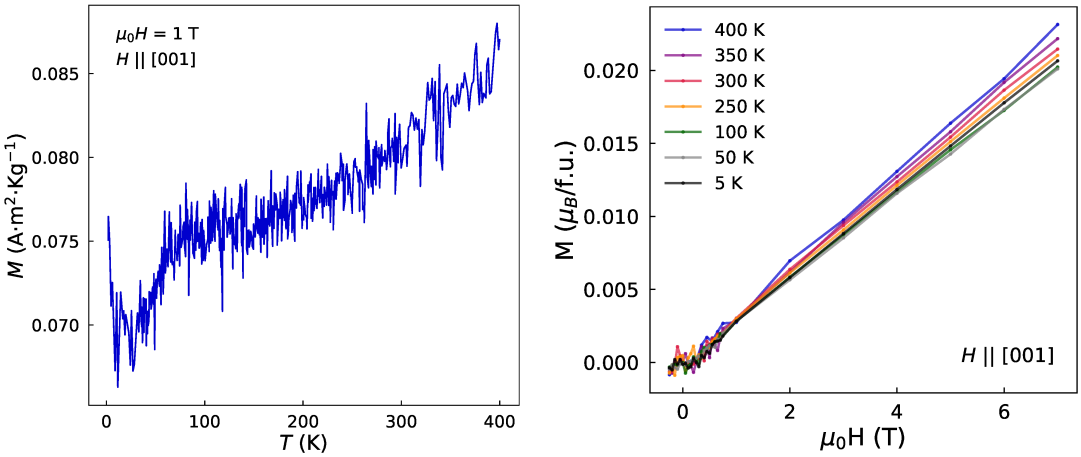

Figure 5.3: Temperature and field dependance magnetization of CuMnAs single crystal grain.

Being below the Néel temperature (T_N = 507 K), temperature dependence of magnetization shows monotonous decrease of magnetization with a drop at $\sim$ 70 K with a minima at $\sim$ 30 K. The minima is not visible in resistivity data (shown further on). Possible explanation for this behavior is due to change of magnetic structure. Yet it is only hypothesis and its proof/disproof would require additional measurement. Below the 320 K the single crystalline grain do not exhibit any sign of FM transition. This further support the statement that the source of FM at T_C = 320 K is of MnAs impurity.

5.2 Electrical resistivity measurement

For the purpose of measuring electrical resistivity, device presented in fig. 4.7 was used.

5.2.1 Temperature dependence of resistivity

Temperature dependence of the the resistivity for 3 different samples (they all share the same design as in 4.7) is shown in fig. 5.4 and fig. 5.5. Typical currents used during the experiments were in the order of 100 μA which results in a current

densities of 2· 10^7 Am^{-2}. The error in calculating the geometrical factor is $\sim$ 15 % due to inaccurate determination of sample thickness.

Notice that c-axis resistance of Sample 1 ρ_{zz} is lower than those corresponding to Sample 2 and Sample 3 while the a-axis resistance ρ_{xx} is higher for Sample 1. This is due to its misorientation and projection of the c-axis resistance into its a-axis component and vice versa. In the case of Sample 2 and Sample 3 the orientation was refined on the FIB/SEM holder by electron backscatter diffraction (EBSD). The reason for the Sample 1 not to be oriented by this method is due to the fact that the used FIB/SEM Tescan LYRA do not have EBSD detector. And the Sample 1 was considered a test Sample for which the exact orientation was not crucial. Therefore for the purpose of orientation by EBSD the FIB/SEM Zeiss Auriga Compact had to be used. In the case of Sample 2 and Sample 3 the resistivities are in an agreement with each other therefore suggesting a good reproducibility of the fabrication process. This shows that FIB micro fabrication with its precise control over sample orientation is crucial when dealing with highly anisotropic materials like CuMnAs. In the following text all of the presented results were measured on Sample 3.

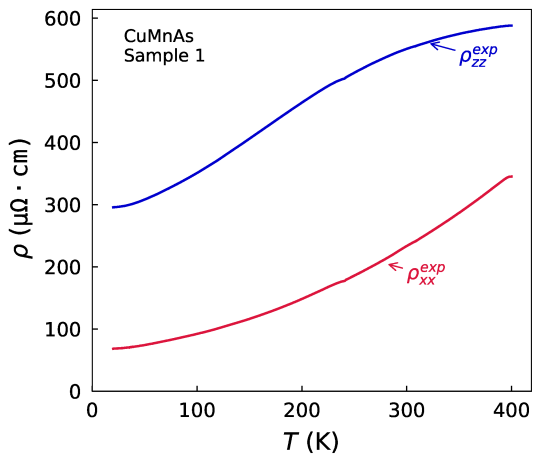

Figure 5.4: Temperature dependence of resistivity for Sample 1.

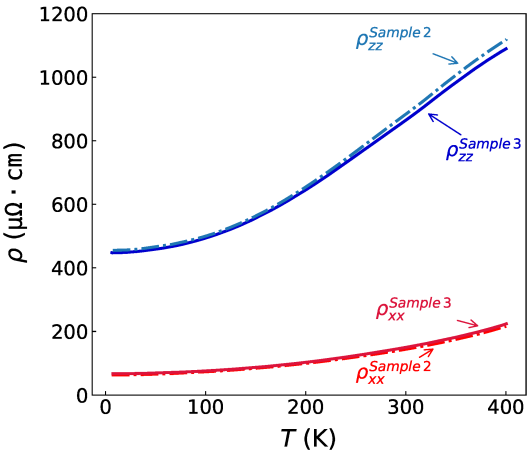

Figure 5.5: Temperature dependence of resistivity for Sample 2 (dashed line) and Sample 3 (full line).

Compared to the thin layers, the a-axis resistivity data ρ_{xx} [10] of our bulk devices shows similar course to those of thin layer [27] with the comparison between their a-axis resistivity at 300 K, 4 K and RRR in table 5.1. The difference can be assigned to a slightly different composition, different quality of the thin layers and the bulk sample or the errors of the sample dimensions. The c-axis resistivity data ρ_{zz} shows monotonous curvature similar to the a-axis resistivity. However a large anisotropy exist between the a-axis and c-axis resistivity (at 5 K the ratio between ρ_{zz} and ρ_{xx} is 6.7) due to the layered structure of CuMnAs. The resistivity for the c-axis is reported for the first time as the thin films geometry (they are grown along [001] direction) doesn't allow so.

	Bulk FIB device	Thin layer
ρ_{xx}^{300K}	149	160
ρ_{xx}^{4K}	67	90
RRR	2.2	1.8

Table 5.1: Comparison between the between the inplane resistivity at 300 K - ρ_{xx}^{300K}, 4 K ρ_{xx}^{4K} and RRR. Values taken from [10], [27]

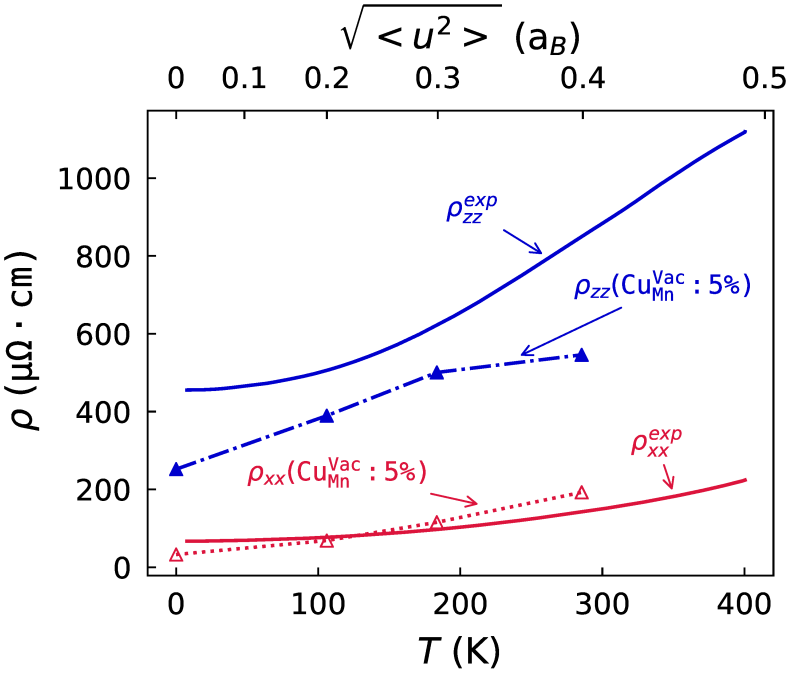

Figure 5.6: Comparison between the experimental data (full line) and microscopic calculations (triangles with a dashed line as a guide for the eye) assuming scattering on static impurities (Cu substituting Mn and vacancies on the Cu site) and phonons. Figure taken from [10]

Theoretical calculations

The comparison between the microscopic theoretical calculations of the resistivity, based the tight-binding linear muffin tin orbital method (for more details see [10]), with the experimental data is in the fig. 5.6. The microscopic model assume ρ_0 to originate from the static impurities which comprises of 5 % of Cu substituting Mn and vacancies on the Cu site. The temperature dependence is due to phonons. Although the agreement is fairly good for the lower temperatures, at higher temperatures the scattering on magnons starts to be more prominent and the agreement is worse. Better agreement between the theoretical and experimental data can be achieved at the cost of less realistic model parameters such as impurity concentration [10]. The theoretical calculation are described in more detail in the work of Wagenknecht [39]

Magnetoresitance

In and out of plane transversal magnetoresistance at various temperatures is shown in fig. 5.7. Out of plane magnetoresistance shows increase of resistance with the increase of absolute value of magnetic field. In contrary in-plane magnetoresistance shows negative magnetoresistance at temperatures below 300 K. This behavior can be explained by suppression of spin fluctuations by external field [10] or some kind of free magnetic moments reacting to the external field. However at temperatures above 300 K resistance tends to decrease until $\mu_0 H = 2.5$ T and then starts to increase. This change of magnetoresistance character from negative to positive at 300 K may suggest change of magnetic structure.

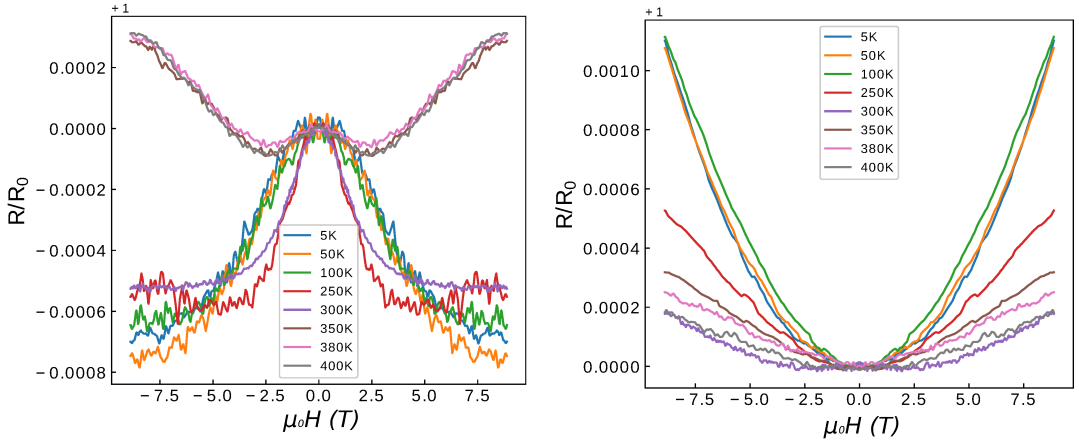

Figure 5.7: Transversal magnetoresistance up to +- 9 T for both a-axis a) and c-axis b) measured at temperatures between 2-400 K.

5.2.2 Anisotropic Magnetoresistance

Angular dependence of resistance on magnetic field is shows in fig. 5.8. The current **j** was injected along the a-axis and the magnetic field was rotated in the ab-plane by an angle ψ. Where $\psi = 0$ denotes **j** $\parallel$ **H** and $\psi = 90$ represents **j** $\perp$ **H**.

Even though of modest magnitude of $\Delta\rho/\rho_0 \sim 0.12\%$ a two-fold symmetry AMR is present. Amplitude is gradually increasing with magnetic field reaching its saturation at about 6 T. Apart from the AMR at $T = 300$ K a tilting of the amplitudes can be observed. This shows clear deviation from $\Delta\rho/\rho_0 \propto cos^2\psi$ which is typical in polycrystalline sample with no magnetocrystalline anisotropy.

Assuming the magnetic structure is identical to the one in the thin layers a microscopic model based on tight binding linear muffin-tin method with the atomic sphere approximation and the component coherent potential approximation can be used (for more details see [10]). Theoretical values of AMR corresponding to various type of static defects are shown in table 5.2.

Comparison between experimental and theoretical data shows that that the order of magnitude is comparable for most of types of the defects. However generally larger theoretical values points out that only a part of the magnetic moments (which are related to the defect) overcomes the magnetic anisotropy by

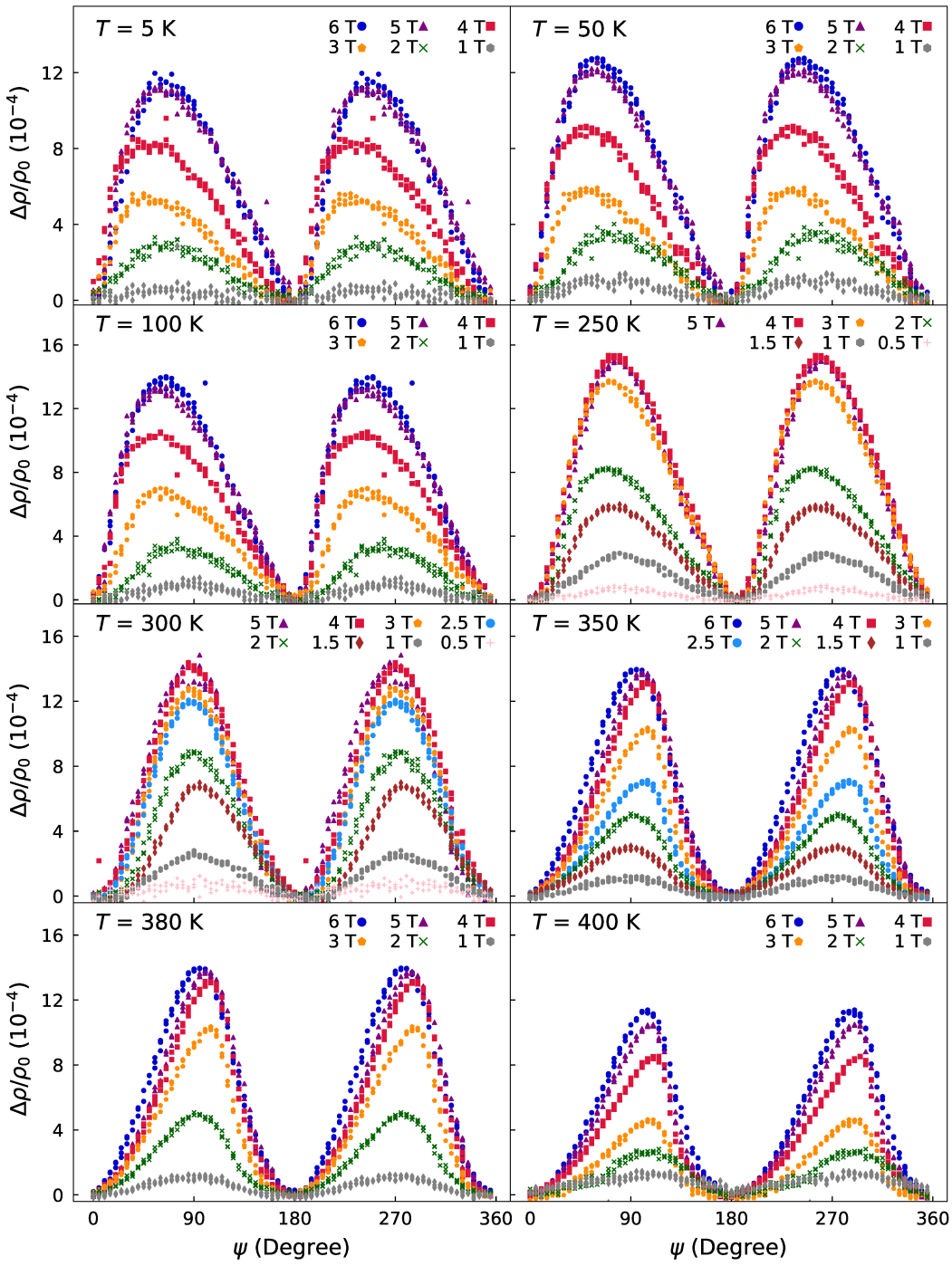

Figure 5.8: Magnetic field direction dependence of AMR at various temperatures. The deviation from $\Delta\rho \sim \cos\psi$ behavior is suppressed at temperature of around ~ 300 K.

	Fully rel., spd		Fully rel., spdf	
Defect	$U = 0$	$U = 0.10$ Ry	$U = 0$	$U = 0.10$ Ry
Vac_{Mn}	$6.09{\cdot}10^{-3}$	$1.16{\cdot}10^{-2}$	$-2.08{\cdot}10^{-4}$	$2.01{\cdot}10^{-2}$
Vac_{Cu}	$-1.04{\cdot}10^{-2}$	$1.08{\cdot}10^{-2}$	$5.24{\cdot}10^{-3}$	$-1.85{\cdot}10^{-2}$
Mn_{Cu}	$2.52{\cdot}10^{-3}$	$6.25{\cdot}10^{-4}$	$2.29{\cdot}10^{-3}$	$1.59{\cdot}10^{-3}$
Cu_{Mn}	$6.69{\cdot}10^{-3}$	$-5.32{\cdot}10^{-4}$	$-2.05{\cdot}10^{-3}$	$1.34{\cdot}10^{-2}$
Cu_{As}	$1.70{\cdot}10^{-3}$	$1.03{\cdot}10^{-3}$	$1.66{\cdot}10^{-3}$	$1.80{\cdot}10^{-4}$
As_{Cu}	$2.79{\cdot}10^{-3}$	$1.05{\cdot}10^{-3}$	$2.42{\cdot}10^{-3}$	$1.13{\cdot}10^{-3}$
As_{Mn}	$3.41{\cdot}10^{-3}$	$1.31{\cdot}10^{-3}$	$1.60{\cdot}10^{-3}$	$1.30{\cdot}10^{-3}$
Mn_{As}	$2.95{\cdot}10^{-3}$	$1.20{\cdot}10^{-3}$	$2.47{\cdot}10^{-3}$	$9.98{\cdot}10^{-4}$
Vac_{Mn}	$2.17{\cdot}10^{-3}$	$1.87{\cdot}10^{-5}$	$2.99{\cdot}10^{-3}$	$2.27{\cdot}10^{-3}$
Cu↔Mn	$2.54{\cdot}10^{-1}$	$2.03{\cdot}10^{-1}$	$2.14{\cdot}10^{-1}$	$1.16{\cdot}10^{-1}$

Table 5.2: Theoretical values of AMR from the microscopic model with 5 % of respective impurity and magnetic moments along [1 0 0]. The Vac_{Mn} means vacancy on Mn site, Mn_{As} represent substition of Mn for As and Cu↔Mn is swap of Mn and Cu. Taken from [10].

the external magnetic field $\mu_0\mathbf{H}$. On the other hand the difference in the case of Cu-Mn swap is so high that it is highly uncommon for those type of defects to occur in our sample or the magnetic moments associated with this type of defect are highly insensitive to the magnetic field $\mu_0\mathbf{H}$.

Stoner-Wohlfhart model

Using Stoner-Wohlfhart model allow us to overcome the fact that it is not clear what really responds to the magnetic field. The procedure for analyzing the data by this model is following. Minimizing the energy (eq. 1.12) at saturation field $\mu_0 H = 6$ T (by assuming that $\beta = 1$) allow us to obtain the canting angle ϕ for a given ψ. Using the eq. 1.31 we fit the experimental data and determine two anisotropy parameters α_2 and $\alpha_2^{'}$. Field dependencies of AMR is achieved by fixing the now known anisotropy parameters α_2, $\alpha_2^{'}$ and changing the β in such way that $\beta = \mathbf{B}\backslash B_0$, where B_0 is saturation field. This fitting procedure was done for the cases of AFM, FM and two domain AFM.and is the same for all of these.

Comparison between the AFM SW model and experimental data at 5 K and 400 K at selected magnetic fields is depicted in fig. 5.9. Anisotropy parameters for the rest of the measured AMR temperatures are plotted in fig 5.10. Modeling at different temperature is in agreement with the direction of easy axis a, being temperature independent while the magnitude of the anisotropy is temperature depend. Further more it flips sign. This behavior is demonstrated in the change of the amplitudes tilts. However the direction of the easy axis $\boldsymbol{a}$ is not aligned along any principal crystallographic direction (i.e. [100], [010])

In the case of FM SW model (fig. 5.11), much worse fit agreement is achieved at fields < saturation field compared to the AFM case. This may suggest that it is not the free magnetic moments or FM impurities such as MnAs nanocrystals that responds to the external field $\mu_0 H$ but more likely an antiferromagnetic coupled magnetic moments. This is consistent with our magnetization data which are

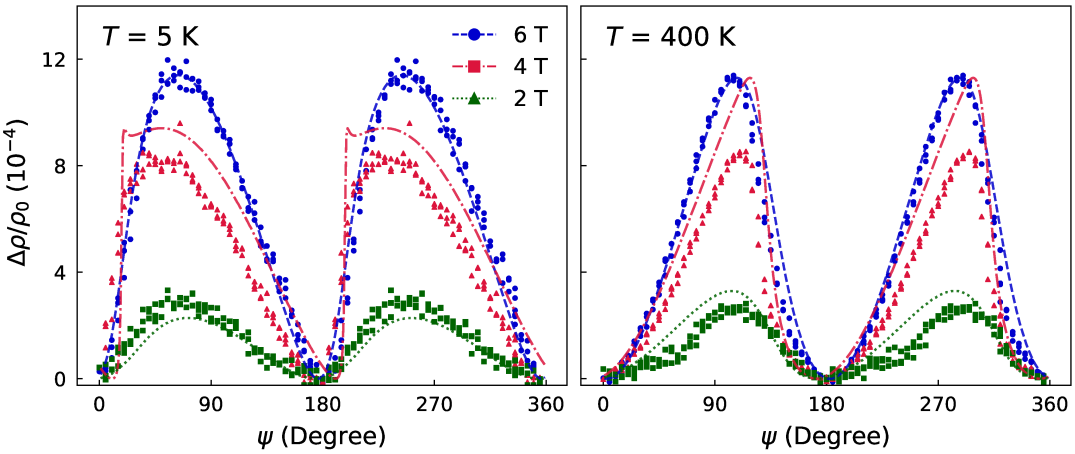

Figure 5.9: SW model for the case of 1 AFM domain. Points represents experimental values, while lines SW model.

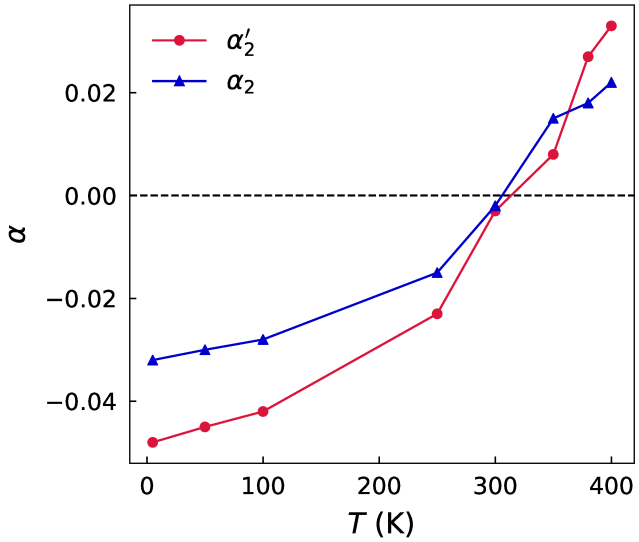

Figure 5.10: Temperature dependence of anisotropic parameters alpha

presented in fig 5.3.

Comparing with the microscopic calculations in table 5.2 it appears that even though we observe antiferromagnetic response, only a fraction of a sample volume is in reality responsible for the AMR signal. Possible scanario involves that the majority of the AFM moments can be pinned down by the structural defects.

If we look back at the anisotropy parameters at 5.10, notice that at 300 K the anisotropy parameters almost vanishes but the saturation field is still present in the experimental data. This would suggest that two or more magnetic anisotropy sources coexist in the sample and the nearly zero anisotropy parameter is a result of averaging of those sources. Considering 2 AFM domains SW model in the ratio 1:1 we can notice (fig. 5.12) that the agreement between the fit and the experimental data is better than in the purely AFM case. Presence of the two AFM domains would explain the two fold AMR. Nevertheless it should be noted that adding more degrees of freedom (in our case 4 anisotropy parameters) during the fitting procedure may lead to a better agreement even if the model is not

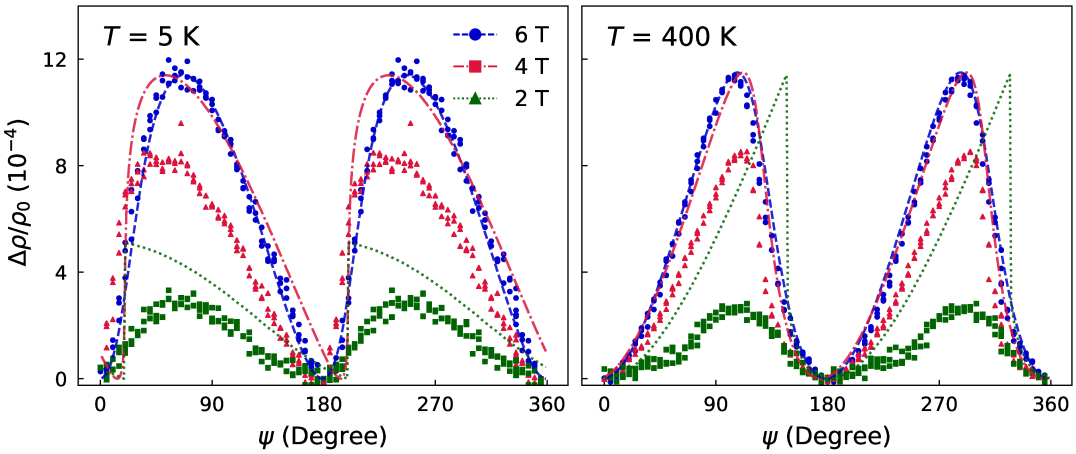

Figure 5.11: SW model for the case of FM domain. Points represents experimental values, while lines SW model.

entirely correct.

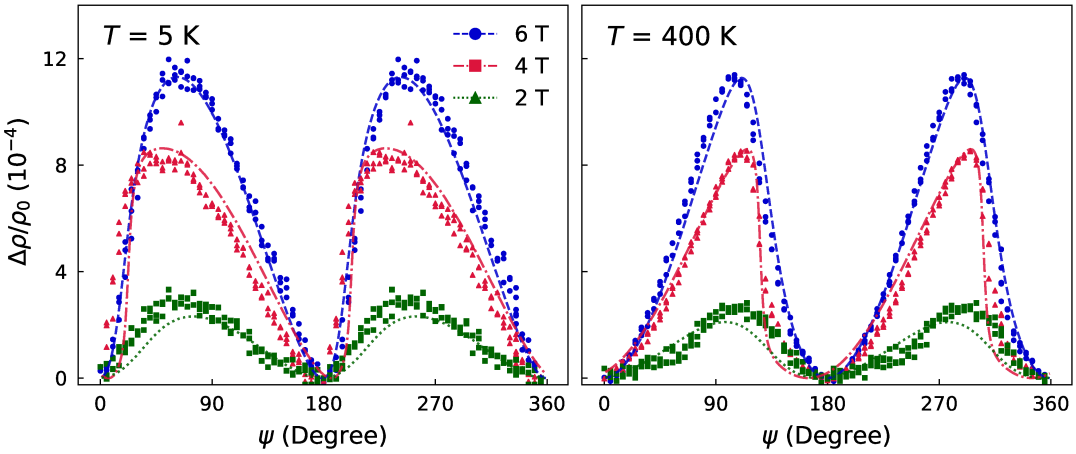

Figure 5.12: SW model for the case of 2 AFM domains Points represents experimental values, while lines SW model.

The two antiferromagnetic domains are to be expected in CuMnAs as it is a tetragonal system where the magnetic moments can point along two perpendicular crystallographic directions. In the form of thin layers, the domains have already been observed [40]. Therefore it is safe to assume that our sample consist of two AFM domains. The 1:1 ratio assumption is valid if the domain size is small compared to the size of the sample.

Conclusion

We have studied magnetic and electrical transport properties of tetragonal $Cu_{1.02}Mn_{0.99}As_{0.99}$. Magnetization measurement on polycrystalline sample shows antiferromagnetic transition at $T_N = 507$ K and further reveals ferromagnetic transition at $T_C \sim 320$ K. Ferromagnetism is not an intrinsic property of CuMnAs and it is believed to originate from MnAs impurity. The amount of impurity is estimated to be of around 1.5-2 %. Magnetization measurement on single crystalline grain chipped out of that polycrystal reveals no FM impurity.

For the purpose of investigating transport properties of tetragonal CuMnAs single crystals, microdevices prepared by focused ion beam were used. We have studied temperature dependence of the resistivity, magnetoresistance and anisotropic magnetoresistance.

The values of resistivity along the a-axis are comparable to the thin layers. For the first time we report the values of the resistivity along c-axis, revealing large anisotropy (factor of ~ 7) between both crystallographic directions. This is most likely due to layered structure of tetragonal CuMnAs. The values of resistivity are in a good agreement with the theoretical calculations.

Transversal magnetoresistance along a-axis changes its sign from positive above 300 K to negative below this temperature. On contrary magnetoresistance along c-axis is positive in a whole temperature range. Such change of magnetoresistance sign is probably cause of change of magnetic structure.

Angular scans of resistivity in various magnetic fields and temperatures, reveals the presence of AMR with two fold symmetry. Its magnitude is modest with with values of 0.12-0.16 % with its maximum at ~ 300 K. The change of tilt of the amplitudes from lower angles to higher angles at 300 K supports the idea of change of magnetic structure. Observed tilting of amplitudes can be explained within the phenomenological Stoner-Wohlfhart due to presence of an uniaxial anisotropy not lying along any principal crystallographic axis.

The SW model suggest that it is not the FM moments (for example isolated Mn moments) but the whole AFM system, which react to the external magnetic field. However a single domain AFM case in unlikely. It is most likely that a multidomain AFM case is in play. The magnetic structure determination in the whole temperature range will be subject of further studies.

Bibliography

[1] T. Jungwirth, X. Marti, P. Wadley, and J. Wunderlich. Antiferromagnetic spintronics. *Nature Nanotechnology*, 11(3):231–241, 2016.

[2] J. Železný, H. Gao, K. Výborný, J. Zemen, J. Mašek, Aurélien Manchon, J. Wunderlich, Jairo Sinova, and T. Jungwirth. Relativistic néel-order fields induced by electrical current in antiferromagnets. *Phys. Rev. Lett.*, 113:157201, Oct 2014.

[3] F Máca, J Mašek, O Stelmakhovych, X Martí, H Reichlová, K Uhlířová, P Beran, P Wadley, V Novák, and T Jungwirth. Room-temperature antiferromagnetism in CuMnAs. *Journal of Magnetism and Magnetic Materials*, 324(8):1606–1612, 2012.

[4] W. Bronger, P. Müller, R. Hoeppner, and H. Schuster. Magnetic properties of NaMnP, NaMnAs, NaMnSb, NaMnBi, LiMnAs, and KMnAs, Characterized by Neutron Diffraction Experiments. *ChemInform*, 18, 1987.

[5] Klára Uhlířová, Elen Duverger-Nédellec, Ross H. Colman, Jiří Volný, Barbora Vondráčková, and Karel Carva. The stability and physical properties of the tetragonal phase of bulk CuMnAs antiferromagnet. *Journal of Alloys and Compounds*, 771:680–685, jan 2019.

[6] Charles Kittel. *Úvod do fyziky pevných látek*. Academia, 8 edition, 1985.

[7] N.W. Ashcroft and N.D. Mermin. *Solid State Physics*. Saunders College, Philadelphia, 1976.

[8] J. M. D. Coey. *Magnetism and magnetic materials*. Cambridge University Press, 1985.

[9] `http://www.irm.umn.edu/hg2m/hg2m_c/hg2m_c.html` to 2.1.2021.

[10] J. Volný, D. Wagenknecht, J. Železný, P. Harcuba, E. Duverger-Nedellec, R. H. Colman, J. Kudrnovský, I. Turek, K. Uhlířová, and K. Výborný. Electrical transport properties of bulk tetragonal cumnas. *Phys. Rev. Materials*, 4:064403, Jun 2020.

[11] Jack Bass, William P Pratt, and Peter A Schroeder. The temperature-dependent electrical resistivities of the alkali metals. *Rev. Mod. Phys.*, 62(3):645–744, 1990.

[12] H. Nowotny E. Gratz. Encyclopedia of materials: Science and technology. In *Boltzmann equation and scattering mechanisms*, pages 751–763. ISBN: 0-08-0431526, 2011.

[13] H. Ebert, A. Vernes, and J. Banhart. Magnetoresistance, anisotropic. In K.H. Jürgen Buschow, Robert W. Cahn, Merton C. Flemings, Bernhard Ilschner, Edward J. Kramer, Subhash Mahajan, and Patrick Veyssière, editors, *Encyclopedia of Materials: Science and Technology*, pages 5079 – 5083. Elsevier, Oxford, 2001.

[14] Studijní text k úloze 424 z praktika. `https://physics.mff.cuni.cz/vyuka/zfp/_media/zadani/texty/txt_424.pdf` k 17.12.2020.

[15] Motohiro Uo, Takahiro Wada, and Tomoko Sugiyama. Applications of x-ray fluorescence analysis (xrf) to dental and medical specimens. *Japanese Dental Science Review*, 01 2014.

[16] Yao N. *Focused Ion Beam Systems*. Cambridge University Press, Cambridge, United Kingdom, 2007.

[17] Philip J W Moll. Focused Ion Beam Microstructuring of Quantum Matter. *Annual Review of Condensed Matter Physics*, 9(1):147–162, 2018.

[18] Valouch Jaromír, Brož, Vladimír, Roskovec, Miloslav. *Fyzikální a matematické tabulky*. SNTL, 1980.

[19] Bernd Schmidt and Klaus Wetzig. *Ion–Solid Interactions*, pages 7–31. Springer Vienna, Vienna, 2013.

[20] S RUBANOV and P R MUNROE. FIB-induced damage in silicon. *Journal of Microscopy*, 214(3):213–221, 2004.

[21] Philip J W Moll, Bin Zeng, Luis Balicas, Stanislaw Galeski, Fedor F Balakirev, Eric D Bauer, and Filip Ronning. Field-induced density wave in the heavy-fermion compound CeRhIn5. *Nature Communications*, 6:6663, mar 2015.

[22] Philip J W Moll, Nityan L Nair, Toni Helm, Andrew C Potter, Itamar Kimchi, Ashvin Vishwanath, and James G Analytis. Transport evidence for Fermi-arc-mediated chirality transfer in the Dirac semimetal Cd3As2. *Nature*, 535:266, jul 2016.

[23] Philip J W Moll, Pallavi Kushwaha, Nabhanila Nandi, Burkhard Schmidt, and Andrew P Mackenzie. Evidence for hydrodynamic electron flow in $PdCoO_2$, volume = 351, year = 2016. *Science*, (6277):1061 LP – 1064, mar.

[24] Maja D. Bachmann, G. M. Ferguson, Florian Theuss, Tobias Meng, Carsten Putzke, Toni Helm, K. R. Shirer, You-Sheng Li, K. A. Modic, Michael Nicklas, Markus Koenig, D. Low, Sayak Ghosh, Andrew P. Mackenzie, Frank Arnold, Elena Hassinger, Ross D. McDonald, Laurel E. Winter, Eric D. Bauer, Filip Ronning, B. J. Ramshaw, Katja C. Nowack, and Philip J. W. Moll. Spatially modulated heavy-fermion superconductivity in CeIrIn5. jul 2018.

[25] Jiří Volný. Příprava mikrostruktur pro měření transportních vlastností těžkofermionových sloučenin, Bachelor thesis, MFF UK, 2019.

[26] R. Lawes. Handbook of microlithography, micromachining and microfabrication, volume 1: Microlithography [book reviews]. *Electronics Communication Engineering Journal*, 10(3):114–115, June 1998.

[27] P Wadley, V Novák, R P Campion, C Rinaldi, X Martí, H Reichlová, J Železný, J Gazquez, M A Roldan, M Varela, D Khalyavin, S Langridge, D Kriegner, F Máca, J Mašek, R Bertacco, V Holý, A W Rushforth, K W Edmonds, B L Gallagher, C T Foxon, J Wunderlich, and T Jungwirth. Tetragonal phase of epitaxial room-temperature antiferromagnet CuMnAs. *Nature Communications*, 4(1):2322, 2013.

[28] P Wadley, V Hills, M R Shahedkhah, K W Edmonds, R P Campion, V Novák, B Ouladdiaf, D Khalyavin, S Langridge, V Saidl, P Nemec, A W Rushforth, B L Gallagher, S S Dhesi, F Maccherozzi, J Železný, and T Jungwirth. Antiferromagnetic structure in tetragonal CuMnAs thin films. *Scientific Reports*, 5(1):17079, 2015.

[29] G Wastlbauer and J A C Bland *. Structural and magnetic properties of ultrathin epitaxial Fe films on GaAs(001) and related semiconductor substrates. *Advances in Physics*, 54(2):137–219, 2005.

[30] P Wadley, B Howells, J Železný, C Andrews, V Hills, R P Campion, V Novák, K Olejn\'ik, F Maccherozzi, S S Dhesi, S Y Martin, T Wagner, J Wunderlich, F Freimuth, Y Mokrousov, J Kuneš, J S Chauhan, M J Grzybowski, A W Rushforth, K W Edmonds, B L Gallagher, and T Jungwirth. Electrical switching of an antiferromagnet. *Science*, 351(6273):587–590, 2016.

[31] Klára Uhlířová, Róbert Tarasenko, Francisco Javier Martínez-Casado, Barbora Vondráčková, and Zdeněk Matěj. Synthesis and single crystal study of cumn3as2 and cu2mn4as3. *Journal of Alloys and Compounds*, 650:224 – 227, 2015.

[32] Peizhe Tang, Quan Zhou, Gang Xu, and Shou-Cheng Zhang. Dirac fermions in an antiferromagnetic semimetal. *Nature Physics*, 12(12):1100–1104, 2016.

[33] Eve Emmanouilidou, Huibo Cao, Peizhe Tang, Xin Gui, Chaowei Hu, Bing Shen, Junyi Wu, Shou-Cheng Zhang, Weiwei Xie, and Ni Ni. Magnetic order induces symmetry breaking in the single-crystalline orthorhombic cumnas semimetal. *Phys. Rev. B*, 96:224405, Dec 2017.

[34] Eve Emmanouilidou, Jinyu Liu, David Graf, Huibo Cao, and Ni Ni. Spin-flop phase transition in the orthorhombic antiferromagnetic topological semimetal Cu0.95MnAs. *Journal of Magnetism and Magnetic Materials*, 469:570–573, 2019.

[35] A. Nateprov, V. Kravtzov, J. Heimann, and J. Cisowski. Crystal structure and properties of cumn3as2. *Journal of Alloys and Compounds*, 248(1):98 – 100, 1997.

[36] Manohar H. Karigerasi, Kisung Kang, Arun Ramanathan, Danielle L. Gray, Matthias D. Frontzek, Huibo Cao, André Schleife, and Daniel P. Shoemaker. In-plane hexagonal antiferromagnet in the cu-mn-as system $cu_{0.82}mn_{1.18}As$. *Phys. Rev. Materials*, 3:111402, Nov 2019.

[37] P. J. W. Moll. Private communication.

[38] Yu.S. Koshkid'ko, E T Dilmieva, J Cwik, K Rogacki, D Kowalska, A P Kamantsev, V V Koledov, A V Mashirov, V G Shavrov, V I Valkov, A V Golovchan, A P Sivachenko, S N Shevyrtalov, V V Rodionova, I V Shchetinin, and V Sampath. Giant reversible adiabatic temperature change and isothermal heat transfer of MnAs single crystals studied by direct method in high magnetic fields. *Journal of Alloys and Compounds*, 798:810–819, 2019.

[39] David Wagenknecht. Theory of spin-dependent transport in magnetic solids, Doctoral thesis, MFF UK, 2019.

[40] M. J. Grzybowski, P. Wadley, K. W. Edmonds, R. Beardsley, V. Hills, R. P. Campion, B. L. Gallagher, J. S. Chauhan, V. Novak, T. Jungwirth, F. Maccherozzi, and S. S. Dhesi. Imaging current-induced switching of antiferromagnetic domains in cumnas. *Phys. Rev. Lett.*, 118:057701, Jan 2017.